UNIVERSITY OF CALIFORNIA

Santa Barbara

Hydroclimate Reconstruction of Semi-Arid Central Asia: Insights from a Kyrgyz Speleothem

A Thesis submitted in partial satisfaction of the

requirements for the degree Master of Science

in Earth Science

by

Abby Whitmarsh Letts

Committee in charge:

Professor Syee Weldeab, Chair

Professor Lorraine Lisiecki

Dr. Dorothy Pak

September 2019

The thesis of Abby Whitmarsh Letts is approved.

_____

Lorraine Lisiecki

_____

Dorothy Pak

_____

Syee Weldeab, Committee Chair

September 2019

Hydroclimate Reconstruction of Semi-Arid Central Asia: Insights from a Kyrgyz Speleothem

Abby Whitmarsh Letts

ACKNOWLEDGEMENTS

I would like to thank my advisor Dr. Syee Weldeab for his guidance throughout the course of this project, as well as for his help greatly improving the written and visual presentation of this research. I would also like to thank committee members Dr. Lorraine Lisiecki and Dr. Dotti Pak for their continuous support and feedback. I am grateful for the following people for their invaluable analytical help: Dr. Andrew Kylander-Clark for assistance with the LA-ICP-MS, Dr. David McGee for U-Th dating, Dr. Lorraine Lisiecki for guidance with statistical analyses, Dr. Gareth Seward for EBSD analysis, Dr. Ben Lopez for help with confocal microscopy, and Dr. Roberta Rudnick for use of her optical microscope. Finally, I am grateful for my family and fellow grad students for their continuous moral support.

ABSTRACT

Hydroclimate Reconstruction of Semi-Arid Central Asia: Insights from a Kyrgyz Speleothem

by

Abby Whitmarsh Letts

Semi-arid Central Asia has been identified as a particularly vulnerable region to global climate change. However, model projections for the region have relatively high uncertainty and there is a lack of absolutely dated records to establish the region's climatic history. In an effort to better understand Central Asia's hydroclimate response to changes in radiative and freshwater forcings, this study focuses on a Kyrgyz speleothem (Central Asia) that spans late Marine Isotope Stage (MIS) 10 (343–358 kyr before present). Trace element, fluorescence, and calcite fabric analysis are employed to provide insights into orbital- to decadal-scale Central Asian climate history. We find that fluorescent banding is exclusively present in columnar microcrystalline calcite and interpret these intervals to be wetter than average. Furthermore, changes in calcite fabrics correspond to shifts in trace element concentrations and correlation coefficients. The correlation between Mg and Sr varies from positive to negative depending on fabric type, whereas Mg and P concentrations are negatively correlated throughout the investigated stalagmite. These results are consistent with the concept of prior calcite precipitation (PCP), which predicts high (low) Mg and low (high) P concentrations during relatively dry (wet) periods. Following the concept of PCP, we interpret Mg and P oscillations as shifts in hydroclimate and find that MIS 10 is

characterized by precipitation variability at the multiannual, decadal, centennial, and millennial scale. The short-term oscillations are superimposed on an orbital-scale aridification trend observed in the Mg signal. Comparing our records with those from northern high latitude (north of our study area) and Asian monsoon regions, a consistent picture emerges; an episode of relatively strong Siberian High (cold high latitude) from mid to late MIS 10 most likely caused a southward shift of the Westerlies and intertropical convergence zone (ITCZ), resulting in decreasing precipitation over the cave site and a weak Asian Monsoon respectively. In contrast, millennial-scale episodes of ice rafted debris (IRD) deposition in the North Atlantic correspond with wet phases in Central Asia. In conclusion, a strengthening of the Siberian High and resulting southward shift of the Westerlies and ITCZ provides a consistent and viable mechanism that reconciles northern high latitude, mid latitude (this study), and low latitude (Asian Monsoon) records. The forcings of the documented millennial-scale changes in Central Asian hydroclimate require further investigation but may be associated with the effects of North Atlantic freshwater perturbations on atmospheric circulation. On the other hand, multidecadal-scale oscillations in Central Asian precipitation may be linked to climate mode variability analogous to the modern North Atlantic Oscillation (NAO) and El Niño Southern Oscillation (ENSO).

1. INTRODUCTION

1.1 Central Asia's climatic significance

This study focuses on the reconstruction of glacial hydroclimate in Central Asia during mid to late marine isotope stage (MIS) 10 (343–358 kyr BP). The geographic extent of Central Asia includes the core region (Kazahkstan, Kyrgyzstan, Uzbekistan, Tajikistan, and Turkmenistan), southwestern Central Asia (Iran, Afghanistan, and Pakistan), and northeastern Central Asia (northwestern China and Mongolia) (Fig. 1b). Central Asia is the largest Westerlies-dominated, semi-arid, winter rainfall zone with a 108-year average annual rainfall ranging from 200 mm to 600 mm (1901–2009) (Huang et al., 2012; Mitchell & Jones, 2005). Regional climate is determined by the strength and latitudinal position of the Westerlies, which are in turn modulated by the strength and aerial extent of the Siberian High (Lioubimtseva et al., 2005). Central Asia is a critical region for characterizing hemispheric teleconnections as it is located at the confluence of the Asian monsoon system, Siberian High, and mid-latitude Westerlies, the latter of which link the region to North Atlantic climate variability (Fig. 1a).

Central Asia has also been identified as one of the most vulnerable regions to global climate change (Beurs et al., 2018; Giorgi, 2006; de Sherbinin, 2014) with a projected rise in temperature and an increasing likelihood of droughts (Barlow et al., 2016; Ozturk et al., 2017). However, precipitation projections for this region have high uncertainties due a lack of observational data and the effect of complex regional topography on climate (Fig. 1b) (Christensen et al., 2013). In addition to uncertainty in future projections, understanding of Central Asia's climate history suffers from a lack of high-resolution reconstructions,

particularly during the Pleistocene. Therefore, hydroclimate records of Central Asia, such as this study, are crucial to elucidate how the region responds to variations in radiative forcings.

1.2 Modern climate in Central Asia

In modern-day Central Asia, moisture originates from the North Atlantic, eastern Mediterranean, Black Sea, Caspian Sea, and Aral Sea regions (Aizen et al., 2006). Moisture is transported by the Westerlies and precipitation occurs primarily during boreal winter and spring (December to May). The seasonality and interannual variability of precipitation are controlled by the Westerlies, whose latitudinal position is modulated by the strength and aerial extent of the Siberian High (Aizen et al., 2001; Lioubimtseva et al., 2005). The Siberian High is a high atmospheric pressure system characterized by cold, dry air that develops over northeastern Siberia during boreal winter. Low solar insolation and the associated snow/ice buildup strengthens and extends the Siberian High southward (Panagiotopoulos et al., 2005), shifting the Westerly jet to a more southerly position. As a result, southern Central Asia (northern Afghanistan and Pakistan) receives maximum precipitation during winter (Dec and January). The subsequent retreat of the Siberian High shifts the Westerlies progressively northward, leading to enhanced precipitation over the Pamirs in March, the Tien Shan in April/May, and northeastern Central Asia (northwestern China and Mongolia) in spring and summer (Gerlitz et al., 2018).

In addition to the Siberian High, Central Asian climate is influenced by the North Atlantic Oscillation (NAO) and the El Niño Southern Oscillation (ENSO). Modeling studies and observational data indicate that positive NAO modes and El Niño phases are associated with increased precipitation over southwest Central Asia (Barlow et al., 2002; Gerlitz et al., 2018; Mariotti, 2007; Syed et al., 2006, 2009). The cause for the precipitation increase is

interpreted to be associated with the development of a 500 hPa trough over southwest Central Asia, either due to a strengthened Icelandic Low (positive NAO) or a weakened Siberian High (El Niño phase) (Syed et al., 2006, 2009). When the eastern Mediterranean storm track reaches the low-pressure 500 hPa trough, it strengthens and receives extra moisture from the Mediterranean, Caspian, and Arabian Seas (Syed et al., 2006, 2009).

1.3 Paleoclimate reconstructions

Holocene climate in Central Asia has been reconstructed from numerous stalagmite (Cai et al., 2017; Cheng et al., 2012, 2016; Liu et al., 2019; Wolff et al., 2017) and paleolimnological studies (Chen et al., 2008; Huang et al., 2009, 2014; Lauterbach et al., 2014; Mathis et al., 2014; Schwarz et al., 2017). At the millennial scale, the results of these studies indicate a relatively coherent regional hydroclimate signal within western Central Asia that is climatically distinct from eastern Central Asia, though there is a broad regional trend of a wet mid-Holocene (Chen et al., 2008; Rudaya et al., 2009). Holocene records have also reproduced dominant features of the modern climate system including the correlation between Central Asian precipitation, Siberian High strength, and NAO mode (Wolff et al., 2017). Additionally, the correspondence of Central Asian records to North Atlantic climate variability has been interpreted to reflect the dominant influence of the Westerlies over the region (Lauterbach et al., 2014; Li et al., 2016; Wolff et al., 2017).

Though Holocene hydroclimate has been widely studied in Central Asia, there is a lack of highly resolved records targeting climatically critical intervals during the Pleistocene. Only two absolutely-dated Pleistocene records exist for Central Asian climate: a composite stalagmite record from the Kesang cave (northwestern China) in the modern summer precipitation regime, and a stalagmite record from the Ton cave (Uzbekistan) in the winter

precipitation regime (Cheng et al., 2012, 2016). Whereas the Ton record only spans the last 140 kyr, the composite 500-kyr Kesang record is relatively low resolution (~350 yr) with numerous time gaps between individual records. One such gap is during MIS 10, a notable glacial interval characterized by low eccentricity and dampened precessional variability.

This study presents a speleothem record from the Chil-Ustun (CU) cave in southwestern Kyrgyzstan during late MIS 10 (343-358 kyr BP), and thus closes a critical gap in Central Asian climate history. The high-resolution trace element record (multi-annual- to decadal-scale) coupled with fluorescence and calcite fabric analysis offers the first absolutely dated look into Central Asian hydroclimate during MIS 10. The objectives of this study are to (1) identify glacial hydroclimate variability and its response to the radiative forcings of MIS 10, and (2) analyze teleconnections between Westerlies-dominated Central Asia, monsoonal Asia, and the North Atlantic.

1.4 Regional setting

The Chil-Ustun (CU) cave is located in southwestern Kyrgyzstan at 1026 m altitude (40˚32.075' N, 72˚31.973' E) (Fig 1a). The chamber is overlain by ~80 m of Devonian limestone bedrock, which consists of high-Mg calcite (Weldeab et al., unpublished). Modern arid conditions have led to minimal soil coverage above the cave. Between 2014 and 2015, temperature sensors were placed outside the cave entrance and within the final chamber, recording hourly temperature measurements for 6 months and 1 year respectively. Outside the cave, diurnal temperatures fluctuate between 19 °C and 42 °C in July and between -1 °C and 21 °C in November (Fig. 2a). In contrast, the temperature of last chamber of the cave is remarkably stable with an average value of 14.86 ± 0.03°C (Fig. 2a), which indicates that cave temperature is mainly controlled by bedrock conduction, or that bedrock conduction is

strongly buffering the temperature associated with convective ventilation. The temperature measurements conducted outside the cave between June and November share close similarity with those measured in nearby city Osh, 24 km west of the CU cave. The mean annual temperature in Osh (1881–1997) is 11.52°C (Fig. 2a) (Williams & Konovalov, 2008). The internal cave temperature (14.86 °C) is offset by ~3°C from the Osh temperature (11.52°C) due to differences in measurement conditions (Fig. 2a). Whereas the meteorological station in Osh records temperature in the shade, the internal cave temperature reflects bedrock conduction that is heated at the surface by the sun, and therefore reflects a higher mean temperature. The external cave measurements are similarly ~3°C higher than the Osh average, which is attributed to the temperature sensor being placed in the sun.

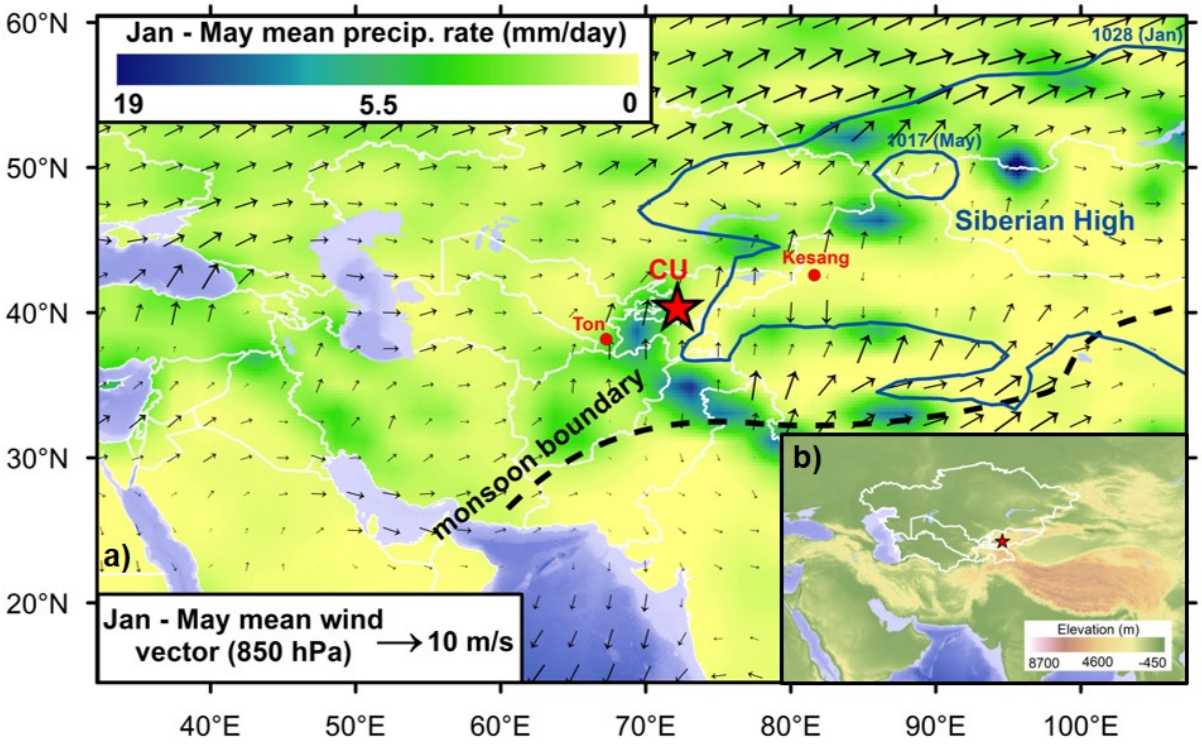

Fig. 1. (a) Seasonal precipitation rate January–May (color shading), wind vectors (arrows), and sea level pressure (blue contours). Data are long-term means from 1981 to 2010 from NCAR reanalysis data (Kalnay et al., 1996) provided by the NOAA/OAR/ESRL PSD, Boulder, Colorado, USA, from their website at https://www.esrl.noaa.gov/psd/. Black dashed line indicates modern extent of the Asian monsoon (Chen et al., 2010). Red star is study site and red dots are the other two Pleistocene stalagmite records (Cheng et al., 2012, 2016). **(b)** Topographic map of the same geographic extent as (a) with core countries of Central Asia outlined in white.

Maximum precipitation over the study area occurs in winter and early spring with an annual average of 363 mm/yr (Fig. 2b) (Williams & Konovalov, 2008). The seasonality and interannual variability of precipitation are controlled by the Westerlies, which are strongly modulated by the strength of the Siberian High. The strengthening of the Siberian High during winter shifts the mid-latitude Westerlies further south, transporting moisture sourced from the North Atlantic, Mediterranean, and Caspian Sea regions to the cave (Aizen et al., 2006).

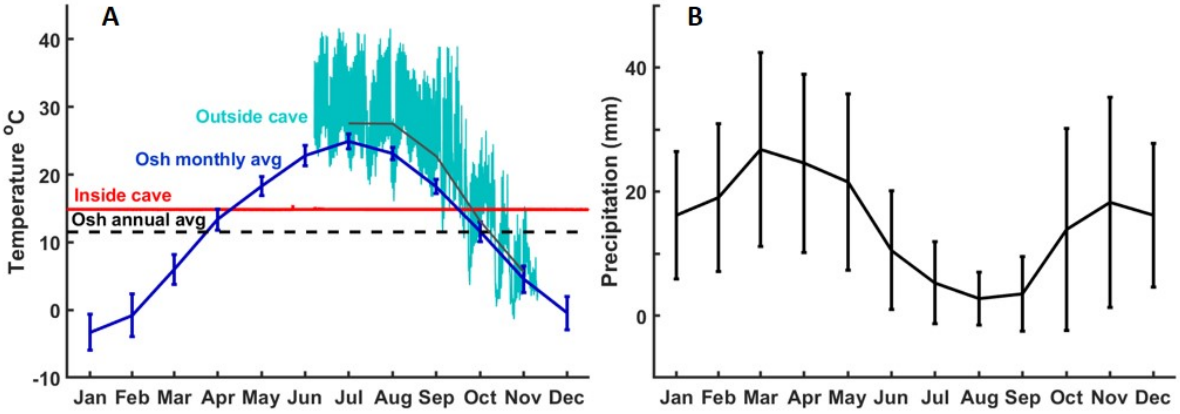

Fig. 2. (a) Hourly air temperature measurements outside (light blue; grey—monthly average) and inside (red) the CU cave (data from Weldeab et al., in prep). Average monthly air temperature of Osh (dark blue) and the annual average (black dashed). **(b)** Average monthly precipitation amount in Osh (black line) and standard deviation (vertical bar). Osh data from Williams and Konovalov (2008), and cave temperature data from monitoring.

2. MATERIALS AND METHODS

2.1 Sample preparation

Stalagmite CU3 was collected ~850 m from the cave entrance in the last chamber of the cave. CU3 was vertically bisected along the growth axis, creating two halves spanning the length of the stalagmite (19 cm). One of the halves was analyzed for trace elements and sampled for $\delta^{18}O$ and $\delta^{13}C$ analysis (Fig. 3a). The complementary half of the stalagmite was bisected along the growth axis. One portion was dated with the U-Th method, and the other half was used create thin sections for calcite fabric and fluorescence analysis (Fig. 3b, c).

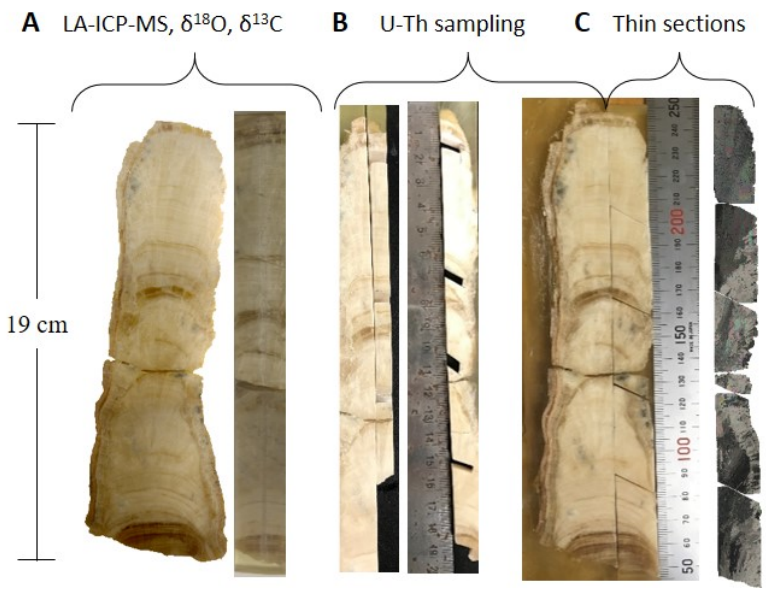

Fig. 3. (a) One half of CU3 sampled along growth axis for trace element and isotope analysis. Complementary half used to sample for U-Th dating **(b)** and to prepare thin sections **(c).**

2.2 U-Th dating

Five solid chip samples (~400 mg) were cut from CU3 using a SYJ-150 Low Speed Diamond Saw (Fig. 3b) and were subsequently prepared and analyzed at the Massachusetts Institute of Technology. Solid chips were sonicated, dissolved in HNO_3, and spiked to achieve a ^{235}U:^{236}U ratio of 2:1. Following a modified procedure of Edwards et al. (1987), spiked samples were prepared using Fe co-precipitation. Ion exchange chromatography with a 200-400 mesh AG1X8 resin was used to separate each sample into a U sample and a Th sample. The U and Th samples for each of the five dating horizons were analyzed on a Nu Plasma II-ES multicollector (MC) inductively coupled plasma mass spectrometer (ICP-MS) to determine ^{238}U, ^{234}U, and ^{230}Th.

^{234}U-^{230}Th ages were calculated using the decay constants for ^{230}Th and ^{234}U as determined by Cheng et al. (2013) and the decay constant for ^{238}U from Jaffey et al. (1971). Ages were corrected for detrital ^{230}Th assuming an initial $^{230}Th/^{232}Th$ of $(4.4 \pm 2.2) \times 10^{-6}$. Estimates of absolute age uncertainty (2σ) include analytical uncertainty and a ±1% uncertainty in the ^{229}Th-^{233}U-^{236}U spike concentration. Absolute ages are used for comparing CU3 to other paleoclimate records. Relative age estimates are used to compare dating

horizons within CU3 that were dated using the same spike. As such, uncertainty in relative age (~0.8%) is lower than absolute age (~1.9%) as the former excludes spike concentration uncertainty.

2.3 Petrography

A FEI Quanta 400f field-emission, environmental scanning electron microscope with an electron backscatter diffraction (EBSD) detector was used to image the section of CU3 spanning 112.5–187.7 mm. EBSD was used to determine the mineralogy and crystal orientation of the stalagmite sample.

Five 30 μm thick thin sections were prepared spanning the vertical extent of CU3. The width of each thin section captures approximately one-half of the width of the stalagmite—from the growth axis to the outer surface. Thin sections were analyzed under an optical microscope for changes in crystal fabrics according to the classification scheme of Frisia (2014).

2.4 Fluorescence

Thin sections for CU3 were scanned for fluorescence intensity using a Leica SP8 Resonant Scanning Confocal microscope with a 405 nm UV excitation source and a 470 nm white light laser line. Overlapping images were obtained with a 10x objective lens and stitched together using Leica software.

2.5 Trace elements

Laser ablation inductively coupled plasma mass spectrometry (LA-ICP-MS) was used to create a ~20 μm resolved time series for Mg, Sr, Ba, P, S, and U. LA-ICP-MS was

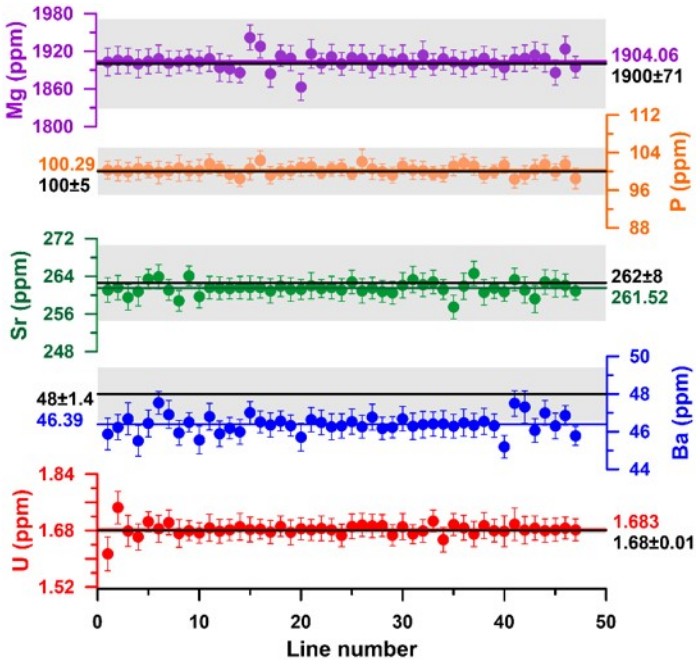

Fig. 4. Average trace element concentrations of standard S-CU5 based on wet chemistry (black lines with grey shading) (wet chemistry data from Weldeab et al., in prep). Trace element concentrations of S-CU5 from LA-ICP-MS line analysis (colored symbols) with standard deviation (error bars). Colored line is the mean of all LA-ICP-MS runs.

performed using an Agilent 7700x coupled to a Photon Machines 193 nm excimer laser with a spot size of 35 µm using line analysis. S-CU5 was used to calibrate the trace element data. S-CU5 is a nano-particulate pressed powder tablet made from a stalagmite from the CU cave (Weldeab et al., in prep). S-CU5 was prepared at the University of Kiel following the method described by Garbe-Schönberg and Müller (2014). The wet chemistry performed on S-CU5 agrees well with the LA-ICP-MS results (Fig. 4). NIST610 was used as a replicate standard during the runs. ^{44}Ca was used as an internal standard to calibrate the trace element data and was artificially normalized to be 40.04 weight percent of the sample.

Outliers were removed based on concentration thresholds. For CU3, samples where Mg>4000 ppm, P>200 ppm, Sr>400 ppm, Ba>125 ppm, U>4 ppm, or S>500 ppm were removed from the interval 0–176 mm. From 176–188 mm, Mg, S, Sr, Ba, and U all peak to their maximum values in the record. Therefore, samples exceeding the concentration thresholds for these elements between 176–188 mm were not considered outliers. Threshold concentrations were determined from the 150-point running mean of the dataset, as well as the range of trace element concentrations in Holocene stalagmites collected from the same cave (Weldeab et al., in prep). P concentrations were significantly noisier than the other trace

elements, and the majority of removed samples were due to the anomalous P concentrations (n=4,015). Of 111,299 samples, 3.7% were removed as outliers (n=4,133). Six distances had duplicates, and the average trace element concentrations of the duplicate distances were used.

2.6 Statistical analysis

CU3 was divided into 11 sections based on transitions in calcite fabrics and trace elements. Pearson correlation coefficients were calculated for the stalagmite as a whole and within individual sections before and after detrending and a ~25 yr smoothing (169-point smoothing). The detrended and smoothed data yielded higher correlation in all cases, and these r-values are reported.

Trace element data are reported before and after first order detrending. Raw data are reported to analyze long-term trends, whereas detrended data are used to highlight centennial- to millennial-scale changes. After detrending, the mean of each section of CU3 was calculated for Mg, Sr, Ba, P, U, and S. Trace elements were analyzed as an anomaly relative to the mean.

Cross wavelet transform and wavelet coherence were performed for Mg-Sr, Mg-P, Mg-S, and S-P according to the method described by Grinsted et al. (2004). As the probability density function (pdf) for each trace element is not normally distributed, the time-series were transformed into percentiles (yielding rectangular pdfs) and standardized to have zero mean and unit standard deviation prior to wavelet analysis. Using the software package from Grinsted et al. (2004), the Morlet wavelet was applied as a band-pass filter for the time series, and a step size of five years was used. A cone of influence was determined where edge artifacts cannot be ignored. The significance of wavelet power is based on a background red noise assumption modeled with a first order autoregressive process. For wavelet

coherence, Monte Carlo methods are used to determine the statistical significance (Grinsted et al., 2004).

Principal component analysis (PCA) was performed on the six trace elements. Prior to PCA, each trace element data set was scaled to have a mean of zero and standard deviation of one in order to equally weight variability in trace elements with different concentrations (e.g. ppm versus ppb). Linear combinations of the input variables (trace elements) were used to create new variables (principle components) that describe the variance of the data in 6-dimensional space. The principal components (PC) are orthogonal to one another and the slope of each PC is given by the coefficients for the six input variables (trace elements). These coefficients are referred to as loads. The score is where each sample in the data set plots along the PC (i.e. the location of the sample along the new axis). The scores, loads, and percent variance explained by the first three PCs were calculated.

3. RESULTS

3.1 Chronology

The age model of CU3 is based on the results of U-Th dating (Table 1). Ages are in stratigraphic order, with the exception of an age reversal at 66.4 mm for sample CU3B (Table 1, Fig. 5). The age reversal may be due to the difficulty of dissolving the large chip samples (~400 mg) and taking them through chemistry (as described in methods). Another possibility is that U loss in CU3B makes the sample's U-Th date appear anomalously old.

Sample ID	Depth (mm)	^{238}U (ng/g) [a]	^{232}Th (pg/g) [a]	$\delta^{234}U$ (per mil) [b]	($^{230}Th/^{238}U$) activity	$^{230}Th/^{232}Th$ (ppm atomic)	Age (yr) (uncorrected) [c]	Absolute age (yr) (corrected) [d]	Relative age (yr) (corrected) [d]	$\delta^{234}U$ initial (per mil) [e]
CU3X	8.5	1704 ±34	1558 ±39	83.1±1.3	1.02668 ±0.00478	17823 ±277	284407 ±6291	284321 ±6291	-	185±4
CU3A	14	1042 ±21	421±8	61.7±0.6	1.03626 ±0.00201	40726 ±20	343693 ±4745	343682 ±4745	343682 ±2074	163±3
CU3B	66.4	1039 ±21	80±2	49.5±0.5	1.03424 ±0.00202	214331 ±170	379411 ±6615	379409 ±6615	379409 ±2769	144±3
CU3C	102.9	838 ±17	168±3	41.7±0.5	1.01557 ±0.00200	80437 ±52	355509 ±5411	355503 ±5411	355503 ±2366	114±2
CU3D	146.5	1033 ±21	41±1	45.1±0.6	1.02045 ±0.00205	403769 ±692	356632 ±5599	356631 ±5599	356631 ±2712	124±3
CU3E	184	1469 ±29	7505± 150	30.0±0.5	1.02680 ±0.00202	3191 ±2	463548 ±14864	463409 ±14865	463409 ±6534	111±5

Table 1. U-Th dating results with 2σ error are reported. [a] Reported errors for ^{238}U and ^{232}Th concentrations are estimated to be ±1% due to uncertainties in spike concentration; analytical uncertainties are smaller. [b] $\delta^{234}U = ([^{234}U/^{238}U]_{activity} - 1) \times 1000$. [c] $[^{230}Th/^{238}U]_{activity} = 1 - e^{-\lambda_{230}T} + (\delta\,^{234}U_{measured}/1000)\,[\lambda_{230}/(\lambda_{230} - \lambda_{234})]\,(1 - e^{-(\lambda_{230} - \lambda_{234})T})$, where T is the age. "Uncorrected" indicates that no correction has been made for initial ^{230}Th. [d] Ages are corrected for detrital ^{230}Th assuming an initial $^{230}Th/^{232}Th$ of (4.4±2.2) x 10^{-6}. [e] $\delta^{234}U_{initial}$ corrected was calculated based on ^{230}Th age (T), i.e., $\delta^{234}U_{initial} = \delta^{234}U_{measured}\ X\ e^{\lambda_{234}*T}$, and T is corrected age. Decay constants for ^{230}Th and ^{234}U are from Cheng et al. (2013); decay constant for ^{238}U is 1.55125 x 10-10 yr^{-1} (Jaffey et al., 1971).

Samples CU3A–E were dated following the methods described in this study. The age of sample CU3X is from a preliminary age screening carried out with the aim to obtain quick but less precise age estimates of the top and bottom of CU3. As a result, in spite of the sample's younger age, CU3X has a higher absolute age uncertainty (2.2%) compared to CU3A–E (1.9%). Although there is uncertainty associated with CU3X (8.5 mm), the sample is included as it indicates a likely growth hiatus between 8.5 mm and 14 mm. The implied growth rate between these dating horizons is 0.093 μm/yr, which is significantly slower than the range observed in stalagmites (1μm – 1mm per year) (Fairchild & Baker, 2012). Additionally, there is likely a growth hiatus between 146.5 mm and 184 mm as the ages imply a growth rate of 0.35 μm/yr. Based on transitions in calcite fabrics (Fig. 5), two growth hiatuses are assumed at 10 mm and 176 mm. Therefore, the age model was created for depths from 10 mm to 176 mm applying linear interpolation of the three U-Th dates at 14 mm,

102.9 mm, and 146.5 mm (Fig. 5). By applying a linear interpolation, an assumption is made that there is no change in growth rate between two adjacent age control points. The growth rate between 14 mm and 102.9 mm (7.52 μm/yr) was extrapolated to 10 mm, and the growth rate between 102.9 and 146.5 mm (38.7 μm/yr) was extrapolated to 176 mm (Fig. 5).

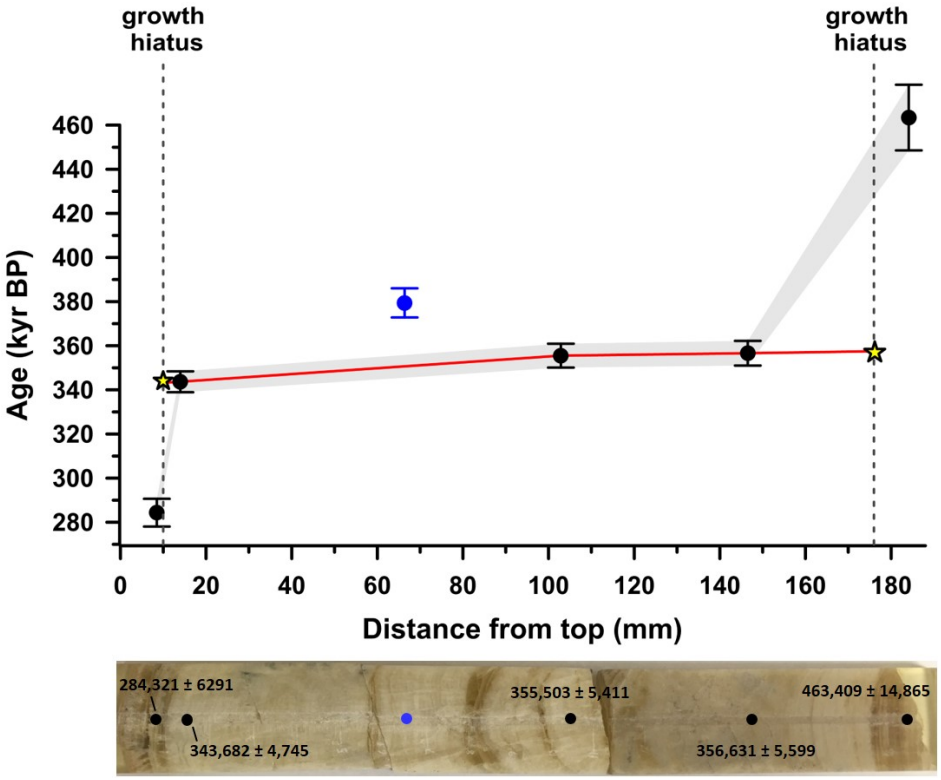

Fig. 5. Age model for CU3 (red line). Black symbols indicate dating horizons, and blue symbol indicates an age reversal at 66.4 mm. Growth hiatuses at 10 mm and 176 mm (dashed lines, stars) are assumed. Note: the growth rate between 14 mm and 102.9 mm was extrapolated to 10 mm, and the growth rate between 102.9 and 146.5 mm was extrapolated to 176 mm.

3.2 Petrography

EBSD analysis shows that CU3 is composed of relatively large calcite crystal grains that extend across growth laminae (Fig. 6a, b). The c-axis of each individual calcite crystal is oriented roughly parallel to the stalagmite growth axis (Fig. 6b, d). The purple and green crystal grains in Figs. 6b–d reflect different rotations about the c-axis. EBSD analysis suggests only sparse, isolated points as aragonite. Adjacent points tend to have different

orientations, and thus likely do not indicate aragonite crystals, but rather are spurious data (Fig. 6c).

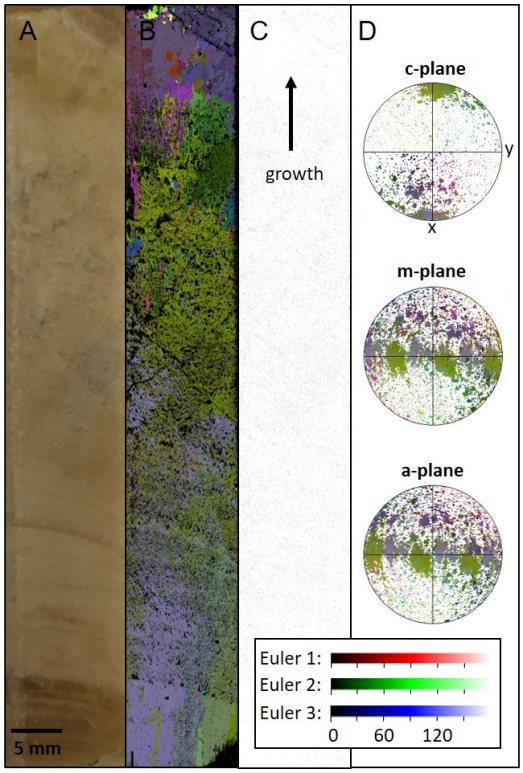

Fig. 6. (a) Scanned image of CU3-3 (112.5–185.5 mm). EBSD map for calcite **(b)** and aragonite **(c)**. **(d)** Pole figures for calcite for the c-plane (top), m-plane (center), and a-plane (bottom). Euler color key: each pixel color is a proportion of red, green, and blue. The color scale wraps around, thus a seemingly large color difference (i.e. green and purple) indicate grains of a similar orientation.

Transitions in color and/or porosity are observed in CU3 at 10 mm, 58.5 mm, 79 mm, 83 mm, 97 mm, 112.5 mm, 120.5 mm, 155.5 mm, and 176 mm. As detailed below, a significant transition in trace element concentrations at 40 mm marks an additional section. Darker laminae (0–10 mm, 79–83 mm, 97–98 mm, 176–188 mm) and the light brown laminae between 112.5–120 mm are less porous. The transitions visible in hand sample are accompanied by changes in calcite fabrics. In CU3, dark brown laminae correspond to columnar microcrystalline fabric (Fig. 7), whereas the white, opaque intervals are characterized by porous fabrics such as columnar open and dendritic fabrics according to the classification scheme of Frisia (2014).

3.3 Fluorescence

Fluorescent banding is exclusively present in darker laminae that are characterized by columnar microcrystalline fabrics. In contrast, intervals with white, porous laminae lack distinct banding (Fig. 8). The fluorescent banding is jagged, tracing out the tips of crystallite growth (Fig. 8a).

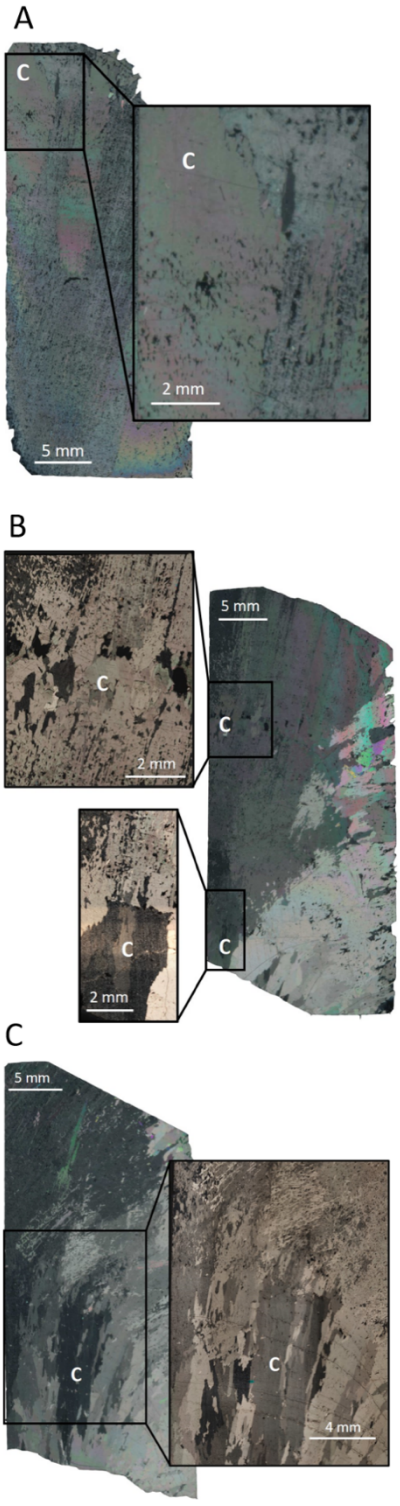

Fig. 7. Thin sections of CU3 in cross polarized light with columnar microcrystalline fabrics denoted as 'C' for distances 5 mm to 42 mm **(a)**, 44 mm to 79 mm **(b)**, and 154 to 188 mm **(c)**.

3.4 Trace elements

Trace element concentrations fluctuate on orbital to decadal scales and tend to follow changes in calcite fabrics (Fig. 9). Each trace element exhibits significant shifts in concentration such that the maximum value of the 150-year moving mean nearly doubles or more than doubles the minimum concentration of the 150-year moving mean. The approximate range of the moving mean for each trace element is as follows: Mg (1100 – 2050 ppm), Sr (120 – 210 ppm), Ba (25 – 55 ppm), P (40 – 100 ppm), U (0.95 – 2 ppm), and S (175 – 290 ppm).

The correlation between trace elements at different time scales is quantified and depicted using Morlet wavelet analysis. Changes in Mg and P concentration are negatively correlated at the millennial-scale, as evidenced by low (high) Mg concentrations in a given section corresponding to high (low) P concentrations (Fig. 9a, d). Wavelet coherence supports this observation and indicates that Mg and P are significantly negatively correlated on timescales as short as the decadal scale, though they are most consistently and

strongly negatively correlated at the millennial scale (Fig. 10a). In terms of Mg and Sr, there is an orbital-scale trend in both time series towards increasing concentrations, though millennial-scale peaks and troughs are not consistently correlated (Fig. 9a, b) as highlighted by the results of wavelet coherence. Although the correlation is predominantly negative, there are times when the correlation coefficient is positive, or the Mg time series exhibits a significant lead over the Sr time series (Fig. 10b). Ba exhibits similar centennial-scale fluctuations as Sr but has an opposing orbital-scale trend towards lower concentrations (Fig. 9b, c). This relationship is mirrored in wavelet coherence, which shows that Ba and Sr are positively correlated on multi-centennial to decadal scales yet lack a long-term correlation on millennial timescales (Fig. 10c). The correspondence of peaks and troughs in the U and S time series (Fig. 9e, f) is evident in a significant in-phase (positive) correlation on centennial to millennial scales in wavelet analysis (Fig. 10d).

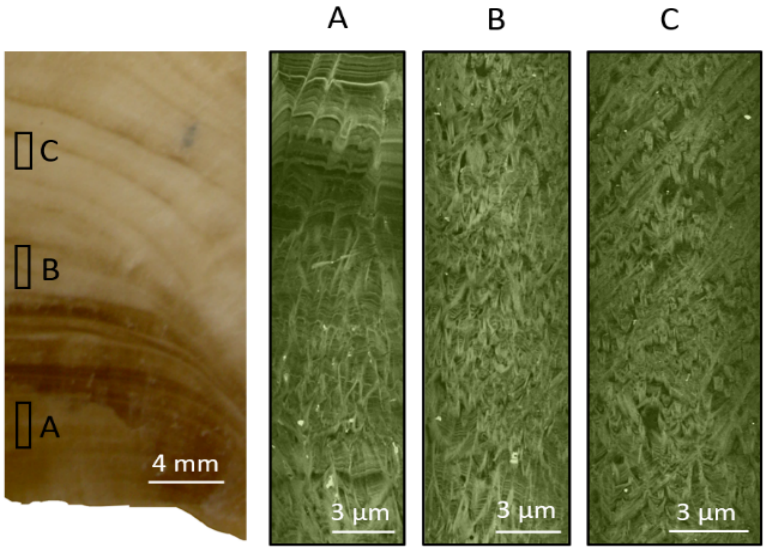

Fig. 8. Left: scanned image of CU3 with boxes indicating portions that are shown for fluorescence. Fluorescence images of CU3 where bright green indicates increased fluorescence for sections **(a)**, **(b)**, and **(c).** Note: prominent fluorescent banding in brown, columnar microcrystalline laminae characterizing all of **(a)**, and at the base of **(b)**. Within predominantly porous intervals, there are fluorescent bands present within the isolated dark laminae.

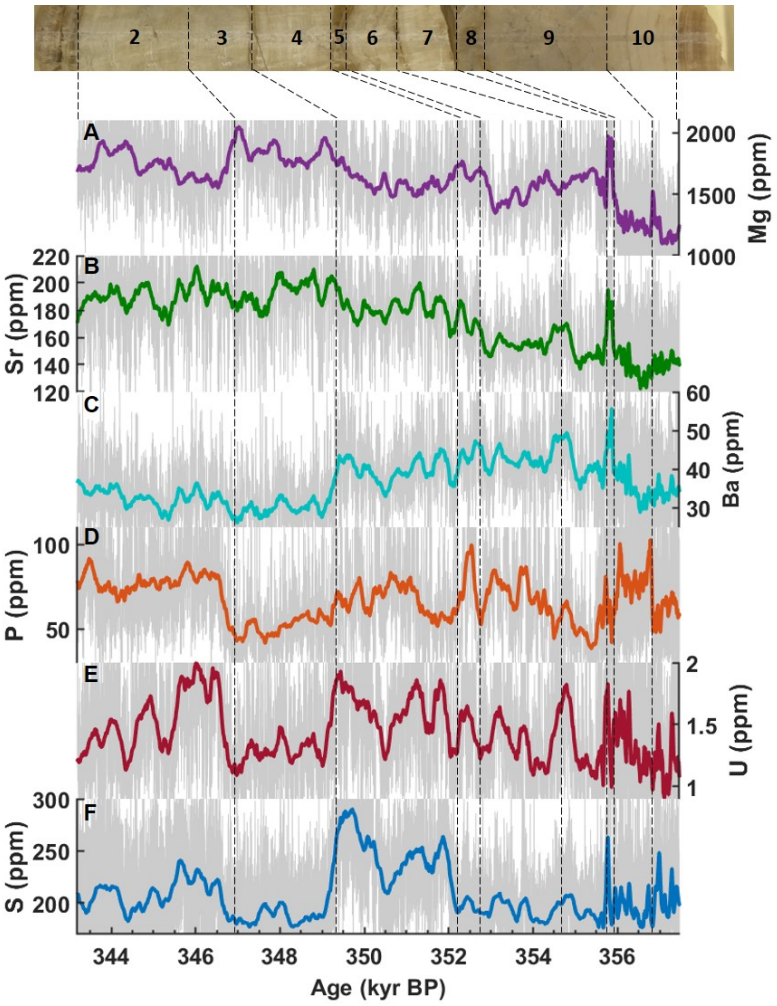

Fig. 9. Top: image of CU3 with dashed lines indicating transitions in calcite fabrics (with the exception of the line at ~347 kyr BP, which denotes a prominent shift in trace elements). Bottom: ~150-yr moving mean of trace elements (color) and raw data (grey) for Mg **(a)**, Sr **(b)**, Ba **(c)**, P **(d)**, U **(e)**, and S **(f)**. Note: sections 1 and 11 not plotted as they lack an age model.

The results of Principal Component Analysis (PCA) are consistent with wavelet analysis. Wavelet analysis reveals that the correlation between trace elements varies depending on timescale, and PCA results similarly vary depending on the degree of smoothing (25-year vs. 150-year moving mean) (Fig. 11). The most prominent difference between the different degrees of smoothing is the PC1 load for Mg, which switches from a low (0.13) to a high (0.39) load with the ~150-year smoothing (Fig. 11b, e). For PC1, Mg and P have lower loads than S, Sr, Ba, and U (25-year), whereas in the case of the 150-year smoothing, Mg has a higher load more similar to S, Sr, Ba, and U (Fig. 11b, e). For PC2, regardless of smoothing Mg and Sr co-vary with one another and are most strongly negatively correlated to P (Fig. 11b, e). For both degrees of smoothing in PC3, Ba has the highest positive load, P has the highest negative load, and the remaining trace elements have loads closer to 0 (Fig. 11b, e). In terms of scores, the time intervals from ~345–347 kyr BP

and 349–352 kyr BP have strong positive scores for PC1, whereas the PC2 score is strongly positive between 347–349 kyr BP (Fig. 11a, d). For the ~25-year smoothing, the percent variance explained by each PC is PC1 (39.15%), PC2 (28.88%), and PC3 (15.28%). For the ~150-year smoothing, the percent variance explained by each PC is PC1 (40.63%), PC2 (27.93%), and PC3(16.68%).

To analyze trace element behavior in different calcite fabrics, Pearson correlation coefficients were calculated between Mg, Sr, Ba, P, U, and S for each section of CU3 (Fig. 12d). The sign and magnitude of the correlation between certain trace elements varies with changes in fabric type. For Mg and Sr, all columnar microcrystalline sections (1, 5, 8, 11) have positive correlations, whereas all porous fabrics exhibit negative correlations (Fig. 12). Additionally, the correlation between U and Sr is consistently positively correlated in all porous fabrics, whereas in three of the four columnar microcrystalline intervals—sections 1, 5, and 8—U and Sr have either no correlation or a negative correlation. On the other hand, regardless of fabric type, Mg and P are consistently negatively correlated and U and S are consistently positively correlated. Ba and Sr exhibit the strongest positive correlations of any two trace elements, with the exception of within the first and last sections (1 and 11).

Notably, section 11 contains anomalous peaks and troughs in trace elements at 183 mm. At 183 mm, Mg and Sr peak to values more than twice as high as any other peak in their respective records, U and S peak to their highest values, Ba reaches its lowest value, and P has a moderate peak. The spikes in Mg, Sr, U, S and the trough in Ba at 183 mm are likely the cause of the lack of correlation in Mg-P, the negative correlation of Ba-Sr, and the positive correlation of U-S in section 11 (Fig. 12d).

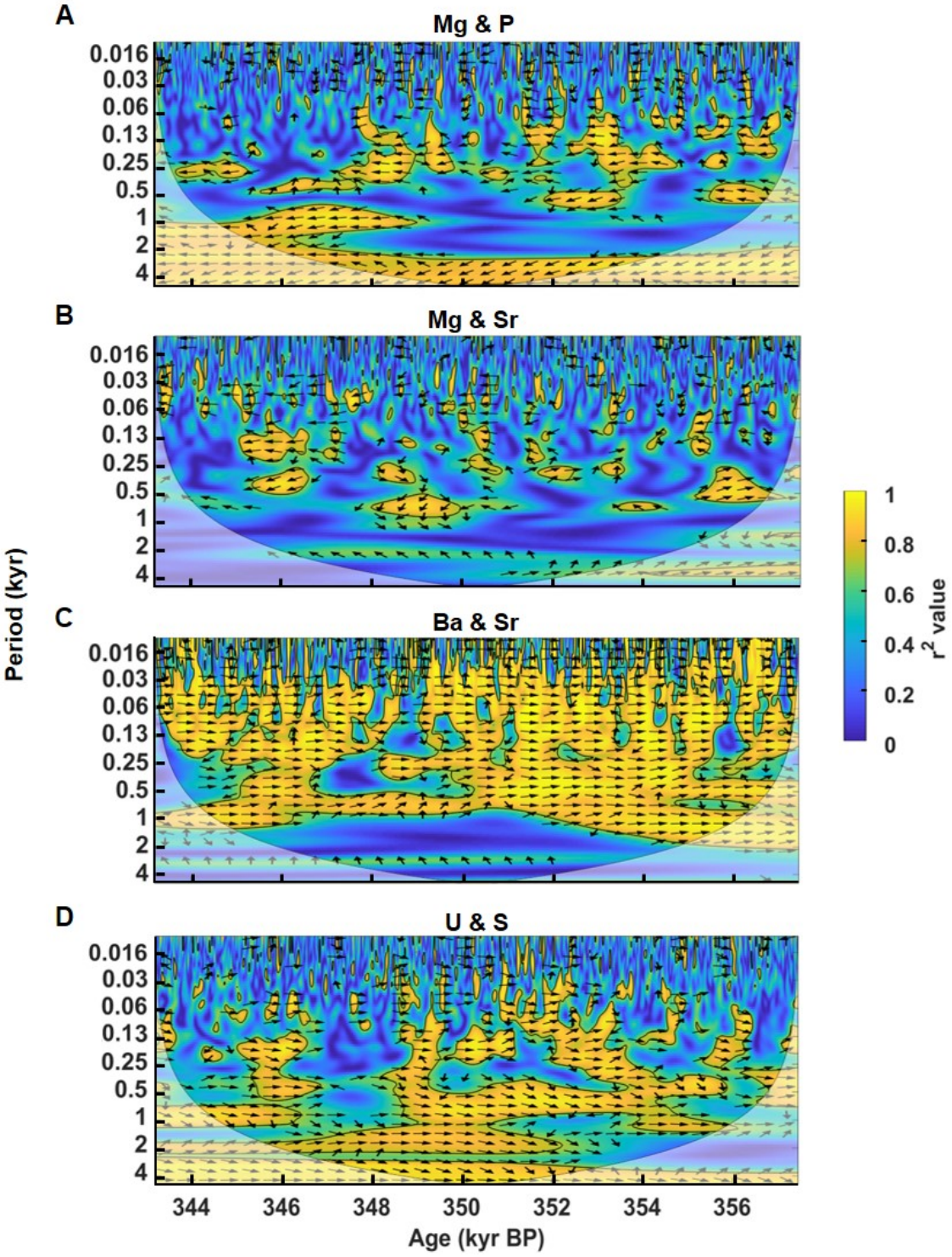

Fig. 10. Wavelet coherence for Mg-P **(a)**, Mg-Sr **(b)**, Ba-Sr **(c)**, and U-S **(d)**. Color bar indicates r^2 value, black contour encloses areas of 95% significance, and cone of influence (grey shading) denotes the area in which edge artifacts cannot be ignored. Left (right) pointing arrows indicate a negative (positive) correlation and downward (upward) pointing arrows indicate time series 1 (2) leads time series 2 (1) by 90 degrees.

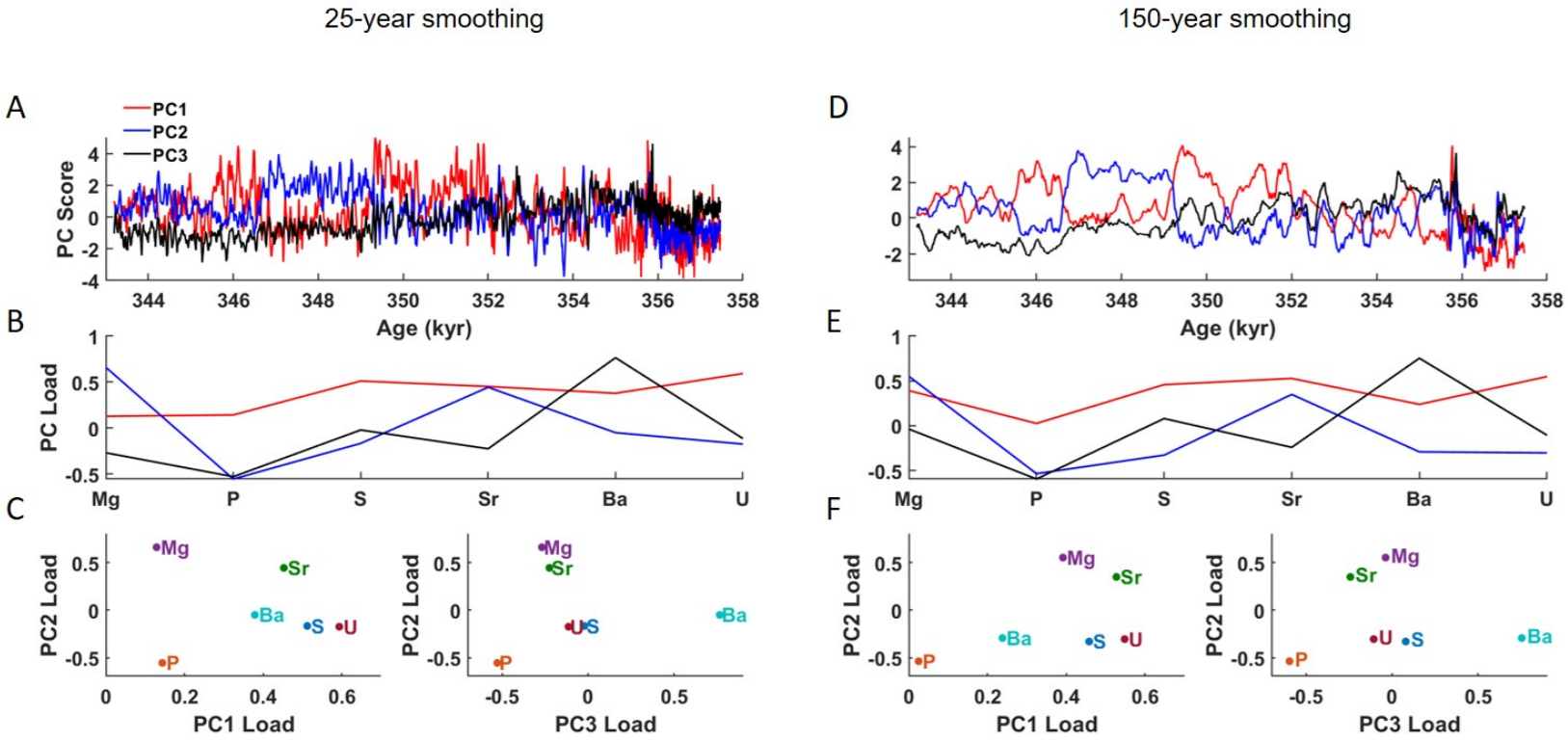

Fig. 11. (a) Scores of each sample for PC1 (red), PC2 (blue), and PC3 (black). For a given PC, a high score indicates the sample has trace elements with high loads for that PC. Positive (negative) scores indicate that samples plot on the positive (negative) side of the PC axis. **(b)** The load of each trace element associated with PC1, PC2, and PC3. A positive (negative) load indicates the trace element is positively (negatively) correlated with the PC. **(c)** PC2 load vs. PC1 (left) and vs. PC3 load (right). Elements that tend to co-vary will have similar loads for PCs and will plot together. **(c, d, e)** Same as **(a, b, c)** but data has been smoothed ~150 years.

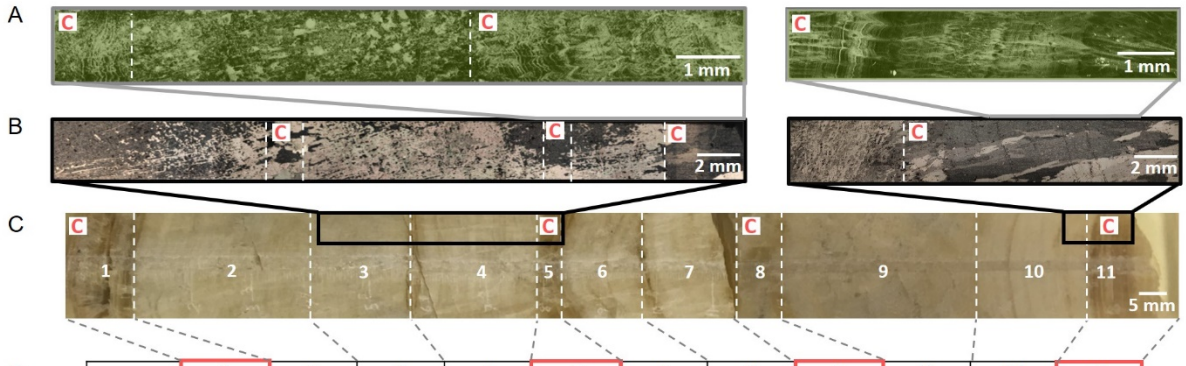

	1	2	3	4	5	6	7	8	9	10	11
Mg-Sr	0.65	-0.51	-0.20	-0.47	0.73	-0.03	-0.44	0.58	-0.21	-0.30	0.85
U-Sr	0.00	0.65	0.49	0.68	-0.30	0.34	0.79	-0.15	0.66	0.57	0.80
Ba-Sr	0.07	0.70	0.87	0.84	0.76	0.91	0.91	0.90	0.81	0.77	-0.64
Mg-P	-0.73	-0.47	-0.54	-0.59	-0.76	-0.70	-0.70	-0.62	-0.54	-0.46	-0.10
U-P	0.53	0.36	0.56	0.37	0.72	0.49	0.70	0.55	0.31	0.17	0.26
U-S	0.72	0.75	0.75	0.75	0.79	0.86	0.77	0.76	0.70	0.59	0.79

Fig. 12. (a) Fluorescence images of CU3 where bright green indicates increased fluorescence. **(b)** Images of CU3 in cross-polarized light. **(c)** CU3 in hand sample. Transitions in calcite fabrics are marked as dashed white lines where 'C' denotes columnar microcrystalline fabric. A significant shift in trace elements, not fabric, defines the transition from section 2 to 3. **(d)** Correlation coefficients between trace elements for each of the eleven sections (~25-year smoothing). Negative correlations are shaded in grey. Sections characterized by columnar microcrystalline fabric are outlined in red.

4. DISCUSSION

4.1 Calcite fabrics and fluorescence

Sharp changes in calcite fabrics and fluorescent banding along the growth axis of CU3 suggest shifts in Central Asia's precipitation during MIS 10. Changes in calcite fabrics in speleothems are interpreted to be associated with changes in environmental conditions including drip rate, Mg concentration of the drip water, degree of degassing, drip water supersaturation, and the presence of impurities (Frisia, 2014). The most abrupt transitions in calcite fabrics occur between the porous fabrics and the columnar microcrystalline fabrics associated with sections 1, 5, 8 and 11 (Fig. 7, 12b). Porous fabrics, such as columnar open and dendritic have been interpreted to form under a conditions of a variable drip rate. On the other hand, columnar microcrystalline calcite is believed to form under a seasonally varying

drip rate and relatively high amount of colloidal material in the drip water (Frisia, 2014). The brown color and highly resolved fluorescent banding in the columnar microcrystalline fabrics of CU3 is most likely associated with the enhanced presence of colloidal organic matter.

Fluorescent banding results from the incorporation of soil-derived organic matter in speleothem calcite (McGarry & Baker, 2000). Bright-dark fluorescent couplets have been interpreted as one annual growth lamina where the bright fluorescent band corresponds to the flushing of soil organic acids at the start of the wet season (Tan et al., 2006). In the context of seasonal infiltration events, the exclusive presence of fluorescent banding in columnar microcrystalline calcite is consistent with the environmental conditions associated with the fabric. The CU3 intervals characterized by columnar microcrystalline fabric and fluorescent banding are interpreted to be wetter than average. Wetter climates are conducive to the development of organic rich soil whose seasonal washout leads to the incorporation of organic matter and PO_4^{3-} in speleothem calcite.

Furthermore, a wet interval would be characterized by a more saturated aquifer. Thus, the pulse of seasonal rainfall may be routed to the cave via fractures in the epikarst, and subsequently be recorded as a fluorescent band. On the other hand, dry intervals that are characterized by matrix flow—seepage flow through primary porosity—may not respond to individual precipitation events (Fairchild & Hartland, 2011). Therefore, the first heavy seasonal rainfall may recharge the aquifer as opposed to being recorded as a distinct fluorescent band. Following this interpretation, porous fabrics lacking fluorescent banding may be indicative of relatively dry episodes. This is consistent with the finding that intervals with reduced precipitation and soil productivity corresponded to weak or absent fluorescent lamination (Rossi et al., 2018).

4.2 Trace elements

Trace element concentrations in speleothems are influenced by the interactions of water with the overlying bedrock, soil above the cave, and the atmosphere (Day & Henderson, 2013; Fairchild & Treble, 2009). Elevated trace element to calcium ratios, particularly Mg/Ca, Sr/Ca, and Ba/Ca in stalagmites can be indicative of prior calcite precipitation (PCP). During dry conditions, reduced infiltration causes increased pore space and air-filled voids in the epikarst. As a result, CO_2 degasses into the air pockets, which drives calcite to precipitate from the reservoir before it reaches the cave. When calcite precipitates, Ca^{2+} in solution decreases and Mg^{2+}, Sr^{2+}, and Ba^{2+} remain relatively unchanged because their partition coefficients are significantly less than 1. Therefore, when the drip water reaches the cave it is relatively enriched in Mg, Sr, and Ba relative to Ca. The calcite that subsequently precipitates on the stalagmite surface will record this geochemical signal, allowing elevated trace element to Ca ratios to be used as an aridity index (Fairchild & Treble, 2009; Stoll et al., 2012; Tremaine & Froelich, 2013).

In contrast to Mg, Sr, and Ba, low values of speleothem P can reflect arid conditions. During PCP, P is removed from drip water as phosphate co-precipitates with calcite (Baldini et al., 2012; Frisia et al., 2012). Furthermore, the phosphate and uranyl ion are correlated due to the precipitation of U(VI) phosphates (Sanding & Bruno, 1992). Due to the co-variance of U and P, Johnson et al. (2006) concluded that during arid conditions with increased PCP, orthophosphate and uranyl ions adsorb to calcite, thus scavenging P and U from the drip water and leading to lower stalagmite P and U. P has also been shown to exhibit cyclic variations due to vegetation dieback, release of phosphates from microbial decomposition of organic matter, and soil washout on a seasonal timescale (Borsato et al., 2007; Huang et al., 2001; Treble et al., 2003). Due to reduced water availability in the dry season, plant roots

take up less phosphate. The subsequent pulse of seasonal rainfall leaches phosphate from the soil, leading to a seasonal spike recorded in the stalagmite.

In this study, trace element data are reported as concentrations, not trace element to calcium ratios. For LA-ICP-MS analysis, ^{44}Ca was normalized to be 40.04 weight percent of the sample as an internal standard to calibrate trace element concentrations. Because the calcium concentration was artificially set to remain constant, trace element to calcium ratios are not reported. In terms of interpreting the record for PCP, reporting concentrations (as opposed to trace element to calcium ratios) has the effect of attenuating variability. For example, in the case of increased PCP, elevated concentrations of Mg, Sr, and Ba would correspond to decreased Ca concentrations, which would amplify the trace element to calcium ratio. Reporting concentrations and assuming constant weight percent Ca would not show this amplification, thus variability in this record may be attenuated.

Prior to interpreting the element time-series in the context of climatically induced PCP, other influences on trace element concentrations were considered. Correlation coefficients and wavelet analysis indicate that Mg and Sr are not consistently positively correlated throughout the stalagmite (Fig. 12d, Fig. 10b). Consistent with the result of Morlet wavelet analyses, the result of PCA analysis (25-year smoothing) shows that Mg and Sr have significantly different loads for PC1 (Fig. 11b). When Sr and Mg are not well correlated throughout a stalagmite it can indicate that the trace element signals are not purely reflecting PCP, and thus are not as reliable as hydroclimate proxies (Tremaine & Froelich, 2013). In semi-arid cave sites, precipitation is less than evapotranspiration and the soil has limited organic matter and nutrient content. As a result, dust and aeolian processes can be a significant source for speleothem Mg and Sr (Belli et al., 2017; Rutlidge et al., 2014). Though dust may play a role in the concentration of Mg and Sr, it would not counteract a

PCP interpretation. During an arid interval, increased dust transport would lead to higher concentrations of Mg and Sr.

Additionally, Mg-Sr variability may be influenced by trace element partition coefficients. The partition coefficient of Mg increases with higher temperatures, whereas partitioning of Sr is not temperature sensitive (Day & Henderson, 2013). Although the CU cave has a constant internal cave temperature (14.86 ± 0.03 °C), on orbital timescales, Mg incorporation is expected to decrease with decreasing temperatures. However, while Northern Hemisphere climate records indicate a long-term cooling from mid to late MIS 10, the Mg record trends towards increasing concentrations (Fig. 13a, c, d, f) (Laskar et al., 2004; Prokopenko et al., 2006). Thus, Mg exhibits the opposite orbital-scale trend as would be expected if temperature was the dominant control on Mg variability.

Finally, growth rate has been shown to increase the partition coefficient of Sr with higher calcification rates in marine analog calcite (Lorens, 1981; Tesoriero & Pankow, 1996), whereas Mg is independent of calcification rate. Given that the development of different calcite fabrics suggests variations in drip rate, Sr may be primarily reflecting growth rate as opposed to PCP. This is supported by the observation that Mg and Sr are exclusively negatively correlated in porous fabrics, whereas in the columnar microcrystalline fabrics they display the expected positive correlation. Similarly, the correlation coefficient between U and Sr varies with fabric type and tends to be weak or negative in columnar microcrystalline fabric, yet positively correlated in porous intervals (Fig. 12). The results of PCA loads indicate that the effect of growth rate on Sr partitioning may be more significant on short timescales. For the ~25-year smoothing, Mg and Sr have significantly different loads for PC1, whereas they have similar loads with a ~150-year smoothing. Additionally, on an orbital scale, both trace elements have a similar trend towards higher concentrations (Fig. 9a,

b). Thus, Sr may be reflecting growth rate on the short-term, but on longer time scales may reflect PCP (Treble et al., 2003).

Other notable trace element relationships include Ba-Sr and S-U. Consistent with previous studies (Ban et al., 2018; Day & Henderson, 2013; Hellstrom & McCulloch, 2000), Ba and Sr share the strongest positive correlation coefficient, which is expected given that they substitute similarly into calcite and have partition coefficients influenced by growth rate (Fig. 12d, Fig. 10c) (Tesoriero & Pankow, 1996). The relationship between S and U has not been extensively explored. However, section correlation coefficients, wavelet analysis, and PC loads all indicate a strong positive correlation between the two trace elements (Fig. 12d, Fig. 10d, Fig. 11c, f). Increased S in speleothems has been interpreted to reflect increased dust input during arid intervals (Cheng et al., 2016; Wolff et al., 2017). However, for the CU cave, the correlation of S with U indicates that S may be primarily sourced from soil organic matter. Ba may also be a primarily soil-derived element as it covaries with P, U, and S in PC2 (Fig. 11). Ba is strongly absorbed to clay minerals in soil and has previously been identified as a soil-derived element in speleothem calcite using PCA (Rutlidge et al., 2014).

Though there are a variety of controls on trace elements, PCA was used to determine variability in the dataset related to hydroclimate. Given a PCP interpretation, time intervals with high (low) concentrations of Mg and Sr and low (high) concentrations of P and U are interpreted to be relatively dry (wet). Additionally, given that S and Ba may be soil-derived, these trace elements would be expected to co-vary with P and U. PC2 reflects these trace element relationships and represents 27.93% of the variability in the data set (150-year smoothing). For PC2, Mg and Sr co-vary with one another and are negatively correlated to P, U, S, and Ba (Fig. 11c, f). As the variability associated with PC2 is consistent with a

hydroclimate interpretation, PC2 is used as an aridity index where strong positive (negative) scores indicate drier (wetter) intervals.

Because Mg and P are consistently negatively correlated throughout the stalagmite and are assumed not to be influenced by growth rate, the time series for these elements are compared to PC2 to interpret hydroclimate shifts during MIS 10 (Fig. 13f–h). The increase of Mg concentration indicates an orbital-scale aridity trend from mid to late MIS 10. Though P does not share the long-term trend indicated by Mg, at the millennial-scale, the strong co-variability of Mg and P indicates oscillations between wet and dry phases. Superimposed on the long-term aridity trend, Mg, P, and PC2 indicate that the intervals from 343–346.5, 349.5–355, and 356–358 kyr BP are relatively wet intervals (Fig. 13f–h).

For analysis of hydroclimate shifts on shorter timescales, Mg and P were detrended, smoothed (~4-yr), and plotted as an anomaly relative to the section mean (Fig. 14a, b). The resolution of the record reveals hydroclimate oscillations at the multi-annual, decadal, and centennial scale. The older half of the record (355.5 to 357.5 kyr BP) has an estimated growth rate of 38.65 μm/yr, roughly five times faster than the growth rate of the younger half of the record (7.52 μm/yr) (343.5 to 355.5 kyr BP). As a result, the older portion of the record is more highly resolved assuming a constant growth rate between age model control points. Wavelet analysis reveals dominant periodicities of 4, 8, 16, 31, 63, and 125 years (Fig. 14c, d). The high frequency hydroclimate oscillations are similar to the multiannual to multidecadal periodicities of the ENSO and NAO (Gámiz-Fortis et al., 2002; Lin, 2007), which suggests that analogous modes of climate variability may be operating during MIS 10.

4.3 Northern Hemisphere climate during MIS 10

The CU3 record spans 343 to 358 kyr BP, approaching the time of peak glacial conditions during MIS 10 (~340 ka) (Lisiecki & Raymo, 2005). During glacial intervals, the Siberian High is interpreted to extend further south and persist longer throughout the year, as the high-pressure cell is strengthened by increased snow and ice cover in northeast Asia (Cohen et al., 2001; Ding et al., 1995). A temperature reconstruction from Lake Baikal (southern Siberia) shows increased cooling from mid to late MIS 10, consistent with a strong Siberian High hypothesis (Prokopenko et al., 2006) (Fig. 13c). Furthermore, a reconstruction of the East Asian winter monsoon (EAWM)—which reflects the movement of cold air originating from the Siberian High—indicates a similar strengthening from mid to late MIS 10, with maximum strength around 340 kyr BP (Hao et al., 2012).

A strengthened and southerly extended Siberian High during late MIS 10 would shift the Westerlies southward, providing a viable explanation for Central Asian hydroclimate changes evidenced in the CU3 records. If the moisture-bearing Westerlies shifted southward of the CU cave, it would reduce precipitation over the study site, consistent with the inferred orbital-scale aridity trend in Mg (Fig 11d). As a consequence, the southward-shifted Westerlies would shift the position of the ITCZ further south, weakening the Asian monsoon system. A trend towards a weakened monsoon from mid to late MIS 10 is indicated by both the global CH_4 concentration record analyzed in Antarctic ice cores and the composite Chinese cave $\delta^{18}O$ record (Cheng et al., 2016; Loulergue et al., 2008) (Fig. 13i, j). Noting that all records presented here harbor millennial-scale age model uncertainties, Figure 13a–j reveals a correlation between episodes of enhanced IRD deposition and sea surface temperature (SST) decrease in the North Atlantic (Barker et al., 2015), lake temperature decrease in Lake Baikal (Prokopenko et al., 2006), air warming over Antarctica (Jouzel et al.,

2007), and humid climate over Central Asia, indicating potential climate links via the bipolar see-saw oscillation.

The longest-duration IRD event during MIS 10 (350 to 353.5 kyr BP) corresponds to an interval of relatively wet Central Asia, cooling at northern high latitudes and warming in Antarctica, consistent with the bipolar seesaw mechanism that links northern and southern hemisphere variability via changes in thermohaline circulation (Broecker, 1998; Shakun et al., 2012). The two other prominent IRD events during MIS 10 (343.2 to 343.4 kyr BP and 355.5 to 357.3 kyr BP) also appear to correlate to a shift towards cooling over Siberia and the North Atlantic, warming over Antarctica, and increased precipitation over Central Asia. The correlation between North Atlantic cooling and wet intervals in the CU records is consistent with previous findings based on a study of Lake Baikal sediment (Murakami et al., 2012) and a peat record from northeastern China (Hong et al., 2014) that link IRD events to cold and wet intervals in Central Asia.

The mechanisms linking IRD events and increased precipitation in Central Asia require further investigation but may be linked to Siberian High strength. IRD events are correlated with extreme northern high latitude cooling (Hemming, 2004) and strong East Asian winter monsoon winds (Sun et al., 2012), conditions that are consistent with a strengthened Siberian High. A paleolimnological study from Lake Baikal over the last 180 kyr has also been interpreted to show increased Siberian High strength during IRD events (Mackay et al., 2013). Furthermore, both Heinrich events (IRD deposition and sea surface cooling in the North Atlantic) and times of a strengthened Siberian High are correlated with an increase of dust transport from Central Asia to Greenland, indicating a teleconnection between North Atlantic cooling and changes in Central Asian atmospheric circulation (Mayewski et al., 1997; Meeker & Mayewski, 2002). Given the established link between

IRD events and increased Siberian High strength, this relationship can likely be applied to the IRD events during MIS 10.

A strengthened Siberian High has a spatially heterogeneous impact on precipitation, but in conjunction with other climate modes it may explain the correlation of wet intervals in Central Asia and IRD events. The CU cave is located approximately between a region of a slight increase in precipitation and a region of a slight decrease in precipitation in response to a strengthening of the modern Siberian High (Gong & Ho, 2002). The precipitation variance in Central Asia explained by the Siberian High, Arctic Oscillation, Eurasian teleconnection pattern, and ENSO is 26%, where the contribution of the Siberian High is 9.8% of that variance (Gong & Ho, 2002). Therefore, while the Siberian High alone is not unequivocally associated with wetter conditions over the cave site, in conjunction with other climate modes it may be casually linked to the increased precipitation shown in the CU records.

Another potential cause of increased precipitation over Central Asia is that the moisture-bearing Westerlies reach maximum strength during IRD events (Jin et al., 2007). However, given that IRD events also correspond to a strengthened Siberian High, the stronger Westerlies may be latitudinally displaced south of the cave site, thus complicating the relationship between Westerly strength and increased Central Asian precipitation. In conclusion, though the exact mechanisms require further exploration, we infer that the large-scale atmospheric circulation changes associated with IRD events are dynamically linked and responsible for increased precipitation over Central Asia.

On shorter timescales, the reconstructed multiannual- to decadal-scale hydroclimate oscillations during MIS 10 have periodicities similar to the ENSO and NAO. Given the modern-day influence of the NAO and ENSO in modulating Central Asian precipitation (Barlow et al., 2002; Gerlitz et al., 2018; Mariotti, 2007; Syed et al., 2006, 2009), the

reconstructed high frequency oscillations between relatively wet and dry conditions in Central Asia suggest that analogous climate modes were likely operating during MIS 10. The centennial-scale variability in the CU3 records is likely controlled by variations in the strength and position of the Siberian High, which shifts the position of the Westerlies. Similar to the mechanisms Perşoiu et al. (2019) invoked to explain drying in Central Asia during the 4.2 ka event, arid intervals in the CU3 records during MIS 10 could be caused by increased sea ice extent, a slowdown of thermohaline circulation, and lowering sea level pressure around Iceland, which would promote a negative NAO phase. The resulting weakened and southward-shifted Westerlies would reduce precipitation over Central Asia.

In summary, the mid-latitude record from the CU cave reconciles climate from low and high latitudes to paint a consistent picture of teleconnections during MIS 10. In the long-term, northern high latitude cooling drives a southward shift of the moisture-bearing Westerlies, thus leading to aridity over the cave site. In comparison, during the extreme cooling associated with IRD events, atmospheric reorganization and the effect of a strengthened Siberian High may lead to increased precipitation over the cave site. Furthermore, high latitude climate records indicate millennial-scale variability consistent with the bipolar seesaw mechanism. As the mid-latitude Westerlies transport North Atlantic climate signal to Central Asia, the pronounced variability in Antarctic temperature and hydroclimate in Central Asia likely present an expression of millennial-scale bipolar climate oscillations similar to that of MIS 2 and 3 (Broecker, 1998; Shakun et al., 2012).

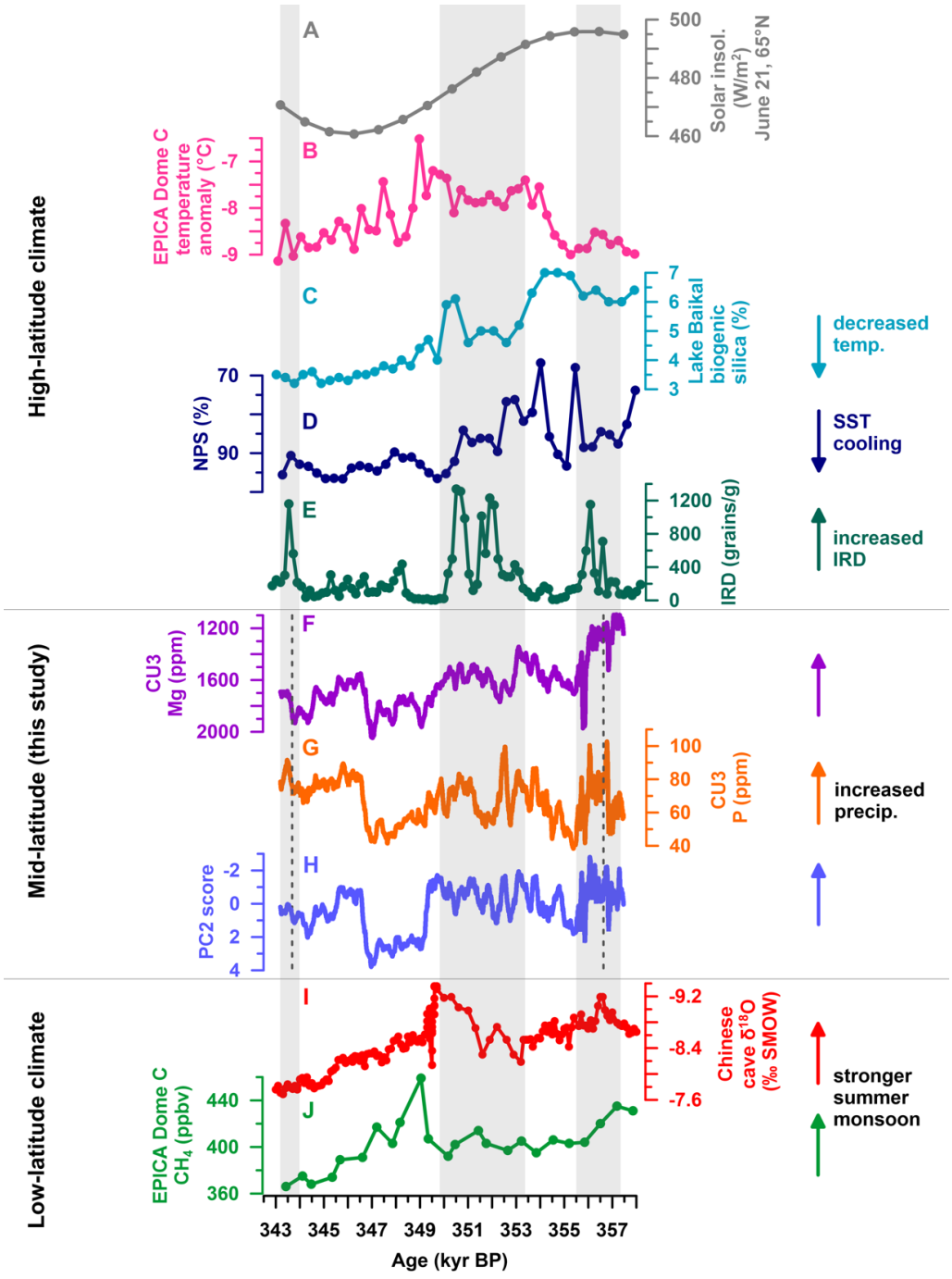

Fig. 13. (a) June 21 solar insolation at 65° N. Insolation data from (Laskar et al., 2004) using AnalySeries software (Paillard et al., 1996). **(b)** Antarctic temperature anomaly (Jouzel et al., 2007) **(c)** Lake Baikal biogenic silica record (Prokopenko et al., 2006). **(d, e)** North Atlantic *N. pachyderma sinistral* record and ice rafted detritus (IRD) record, respectively (Barker et al., 2015). Vertical grey shading indicates IRD intervals. **(f, g)** CU3 record for Mg (purple) and P (orange) respectively. ~150-yr average plotted. **(h)** PC2 score with ~150-year smoothing. Dashed lines indicate portion of CU3 where age model was extrapolated to the early and late ends of the record. **(i)** Monsoonal Asia composite stalagmite $\delta^{18}O$ record (Cheng et al., 2016). **(j)** Antarctic CH_4 record (Loulergue et al., 2008).

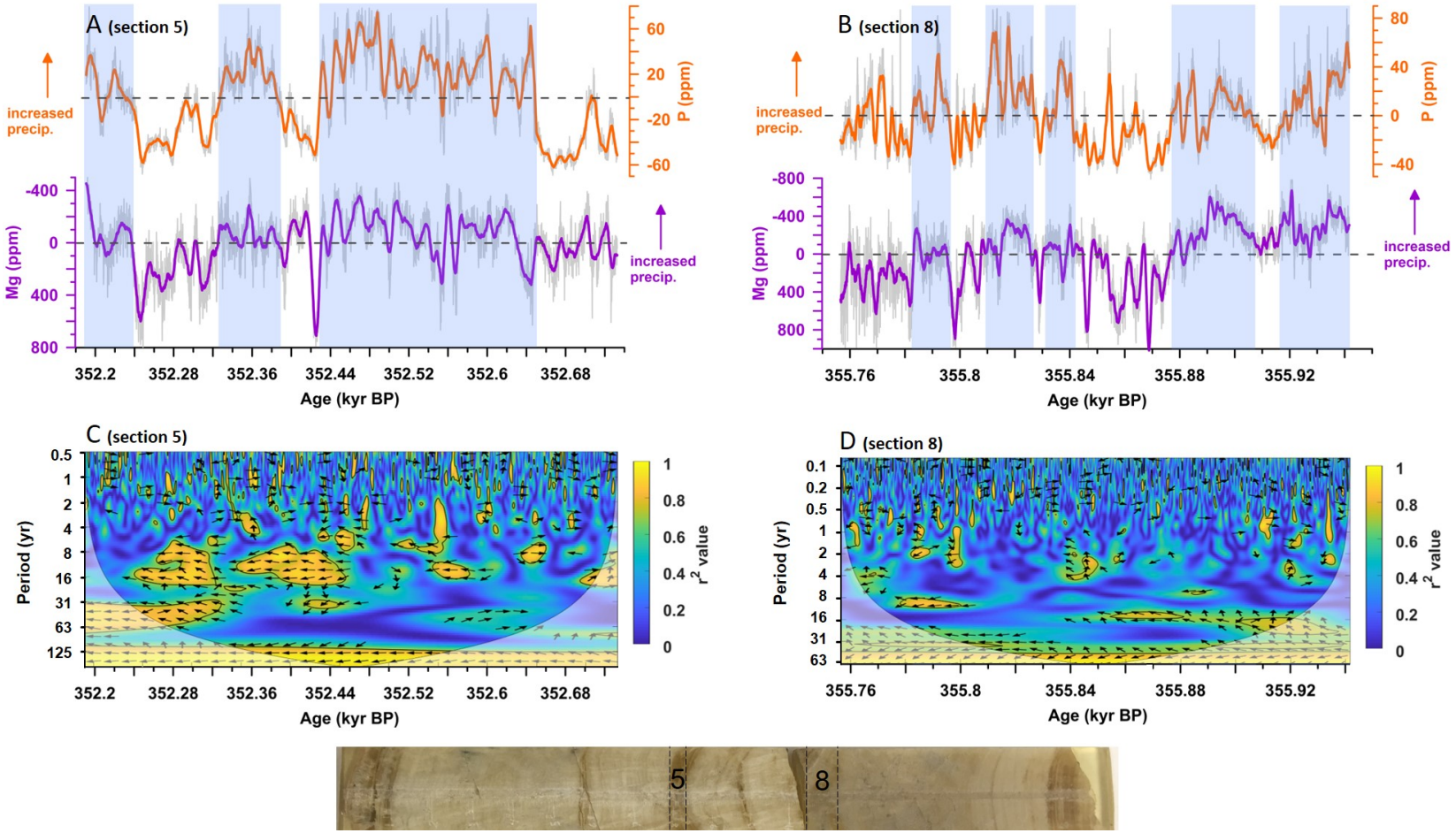

Fig. 14. (a,b) Mg (purple) and P (orange) concentrations after first-order detrending and plotted as an anomaly relative to the section mean for sections 5 **(a)** and 8 **(b)**. ~4-year moving mean (color) and raw data (grey). Blue shading indicates regions interpreted as shifts to wetter conditions. Note: the Mg axis is reversed as low concentrations of Mg indicate increased precipitation according to a PCP interpretation. **(c,d)** Wavelet coherence for Mg-P for sections 5 **(c)** and 8 **(d)**. Color bar indicates r^2 value, black contour encloses areas of 95% significance, and cone of influence (grey shading) denotes the area in which edge artifacts cannot be ignored. Left (right) pointing arrows indicate a negative (positive) correlation and downward (upward) pointing arrows indicate time series 1 (2) leads time series 2 (1) by 90 degrees.

5. CONCLUSION

The paired analyses of trace elements, fluorescence, and calcite fabrics reveal significant shifts in Central Asian hydroclimate during MIS 10. At the orbital scale, Central Asian climate was characterized by an aridification trend, coinciding with decreasing Northern Hemisphere solar insolation. The mechanism driving the aridification trend is likely a southward shift of the moisture-bearing Westerlies in response to a long-term strengthening of the Siberian High. Our findings provide a critical link to put results of northern high and low latitude paleoclimate reconstructions in the context of large-scale, dynamical changes in atmospheric circulation.

Superimposed on orbital-scale drying, the CU3 records indicate significant millennial-scale oscillations in Central Asian hydroclimate that may be linked to fluctuations in northern high latitude climate. Northern hemisphere climate records during MIS 10 indicate that IRD and surface cooling events correspond to decreased temperature over Siberia and increased precipitation over Central Asia. Furthermore, IRD events correspond to increased Antarctic temperatures though correlation of millennial-scale events is associated with a large uncertainty. Given the close link of southern and northern high latitude climate via the bipolar oscillation mechanism, evident in the climate records of MIS 2 and MIS 3, a similar mechanism may be operating during MIS 10.

On multidecadal-to-centennial timescales, the trace element time-series suggest rapid oscillations between relatively dry and wet phases in Central Asia. These high frequency fluctuations indicate that the strength and position of the Siberian High and Westerlies may not have been stable during MIS 10. Additionally, given the modern relationship between

Central Asian precipitation, NAO, and ENSO phase, analogs to these two climate modes may be controlling the short-term oscillations in Central Asian hydroclimate.

In conclusion, although the CU3 precipitation reconstruction is a local record, it allows for a dynamic hemispheric climate interpretation from decadal to orbital timescales. Variability in mid-latitude precipitation provides a crucial link between low and high latitude climate and reveals a consistent mechanism that links climate variability from the arctic to the tropics.

REFERENCES

Aizen, E. M., Aizen, V. B., Melack, J. M., Nakamura, T., & Ohta, T. (2001). Precipitation and atmospheric circulation patterns at mid-latitudes of Asia. *International Journal of Climatology*, *21*(5), 535–556. https://doi.org/10.1002/joc.626

Aizen, V. B., Aizen, E. M., Joswiak, D. R., Fujita, K., Takeuchi, N., & Nikitin, S. A. (2006). Climatic and atmospheric circulation pattern variability from ice-core isotope/geochemistry records (Altai, Tien Shan and Tibet). *Annals of Glaciology*, *43*, 49–60. https://doi.org/10.3189/172756406781812078

Baldini, J. U. L., McDermott, F., Baldini, L. M., Ottley, C. J., Linge, K. L., Clipson, N., & Jarvis, K. E. (2012). Identifying short-term and seasonal trends in cave drip water trace element concentrations based on a daily-scale automatically collected drip water dataset. *Chemical Geology*, *330–331*, 1–16. https://doi.org/10.1016/j.chemgeo.2012.08.009

Ban, F., Baker, A., Marjo, C. E., Duan, W., Li, X., Han, J., et al. (2018). An optimized chronology for a stalagmite using seasonal trace element cycles from Shihua Cave, Beijing, North China. *Scientific Reports*, *8*(1), 4551. https://doi.org/10.1038/s41598-018-22839-z

Barker, S., Chen, J., Gong, X., Jonkers, L., Knorr, G., & Thornalley, D. (2015). Icebergs not the trigger for North Atlantic cold events. *Nature*, *520*(7547), 333–336. https://doi.org/10.1038/nature14330

Barlow, M., Cullen, H., & Lyon, B. (2002). Drought in Central and Southwest Asia: La Niña, the Warm Pool, and Indian Ocean Precipitation. *Journal of Climate*, *15*(7), 697–700. https://doi.org/10.1175/1520-0442(2002)015<0697:DICASA>2.0.CO;2

Barlow, M., Zaitchik, B., Paz, S., Black, E., Evans, J., & Hoell, A. (2016). A Review of Drought in the Middle East and Southwest Asia. *Journal of Climate*, *29*(23), 8547–8574. https://doi.org/10.1175/JCLI-D-13-00692.1

Belli, R., Borsato, A., Frisia, S., Drysdale, R., Maas, R., & Greig, A. (2017). Investigating the hydrological significance of stalagmite geochemistry (Mg, Sr) using Sr isotope and particulate element records across the Late Glacial-to-Holocene transition. *Geochimica et Cosmochimica Acta*, *199*, 247–263. https://doi.org/10.1016/j.gca.2016.10.024

Beurs, K. M. de, Henebry, G. M., Owsley, B. C., & Sokolik, I. N. (2018). Large scale climate oscillation impacts on temperature, precipitation and land surface phenology in Central Asia. *Environmental Research Letters*, *13*(6), 065018. https://doi.org/10.1088/1748-9326/aac4d0

Borsato, A., Frisia, S., Fairchild, I. J., Somogyi, A., & Susini, J. (2007). Trace element distribution in annual stalagmite laminae mapped by micrometer-resolution X-ray fluorescence: Implications for incorporation of environmentally significant species. *Geochimica et Cosmochimica Acta*, *71*(6), 1494–1512. https://doi.org/10.1016/j.gca.2006.12.016

Broecker, W. S. (1998). Paleocean circulation during the Last Deglaciation: A bipolar seesaw? *Paleoceanography*, *13*(2), 119–121. https://doi.org/10.1029/97PA03707

Cai, Y., Chiang, J. C. H., Breitenbach, S. F. M., Tan, L., Cheng, H., Edwards, R. L., & An, Z. (2017). Holocene moisture changes in western China, Central Asia, inferred from stalagmites. *Quaternary Science Reviews*, *158*, 15–28. https://doi.org/10.1016/j.quascirev.2016.12.014

Chen, F., Yu, Z., Yang, M., Ito, E., Wang, S., Madsen, D. B., et al. (2008). Holocene moisture evolution in arid central Asia and its out-of-phase relationship with Asian monsoon history. *Quaternary Science Reviews*, *27*(3), 351–364. https://doi.org/10.1016/j.quascirev.2007.10.017

Cheng, H., Zhang, P. Z., Spötl, C., Edwards, R. L., Cai, Y. J., Zhang, D. Z., et al. (2012). The climatic cyclicity in semiarid-arid central Asia over the past 500,000 years. *Geophysical Research Letters*, *39*(1). https://doi.org/10.1029/2011GL050202

Cheng, H., Edwards, R. L., Shen, C.-C., Polyak, V. J., Asmerom, Y., Woodhead, J., et al. (2013). Improvements in 230Th dating, 230Th and 234U half-life values, and U–Th isotopic measurements by multi-collector inductively coupled plasma mass spectrometry. *Earth and Planetary Science Letters*, *371–372*, 82–91. https://doi.org/10.1016/j.epsl.2013.04.006

Cheng, H., Spötl, C., Breitenbach, S. F. M., Sinha, A., Wassenburg, J. A., Jochum, K. P., et al. (2016). Climate variations of Central Asia on orbital to millennial timescales. *Scientific Reports*, *6*, 36975. https://doi.org/10.1038/srep36975

Cheng, H., Edwards, R. L., Sinha, A., Spötl, C., Yi, L., Chen, S., et al. (2016). The Asian monsoon over the past 640,000 years and ice age terminations. *Nature*, *534*(7609), 640–646. https://doi.org/10.1038/nature18591

Christensen, J. H., Krishna Kumar, K., Aldrian, E., An, S.-I., Cavalcanti, I. F. A., de Castro, M., et al. (2013). Climate Phenomena and their Relevance for Future Regional Climate Change. In: Climate Change 2013: The Physical Science Basis. Contribution of Working Group I to the Fifth Assessment Report of the Intergovernmental Panel on Climate Change [Stocker, T.F., D. Qin, G.-K. Plattner, M. Tignor, S.K. Allen, J.

Boschung, A. Nauels, Y. Xia, V. Bex and P.M. Mdgley (eds.)]. *Cambridge University Press, Cambridge, United Kingdom and New York, NY, USA*.

Cohen, J., Saito, K., & Entekhabi, D. (2001). The role of the Siberian high in northern hemisphere climate variability. *Geophysical Research Letters*, *28*(2), 299–302. https://doi.org/10.1029/2000GL011927

Day, C. C., & Henderson, G. M. (2013). Controls on trace-element partitioning in cave-analogue calcite. *Geochimica et Cosmochimica Acta*, *120*, 612–627. https://doi.org/10.1016/j.gca.2013.05.044

Ding, Z., Liu, T., Rutter, N. W., Yu, Z., Guo, Z., & Zhu, R. (1995). Ice-Volume Forcing of East Asian Winter Monsoon Variations in the Past 800,000 Years. *Quaternary Research*, *44*(2), 149–159. https://doi.org/10.1006/qres.1995.1059

Edwards, R. L., Chen, J. H., & Wasserburg, G. J. (1987). 238U234U230Th232Th systematics and the precise measurement of time over the past 500,000 years. *Earth and Planetary Science Letters*, *81*(2), 175–192. https://doi.org/10.1016/0012-821X(87)90154-3

Fairchild, I. J., & Baker, A. (2012). *Speleothem science: from process to past environments*. Hoboken, N.J: Wiley.

Fairchild, I. J., & Hartland, A. (2011). Trace element variations in stalagmites: controls by climate and by karst system processes. In G. Ferraris, M. Prieto, & H. Stoll (Eds.), *Ion Partitioning in Ambient-Temperature Aqueous Systems* (pp. 259–287). London: Mineralogical Society of Great Britain & Ireland. https://doi.org/10.1180/EMU-notes.10.7

Fairchild, I. J., & Treble, P. C. (2009). Trace elements in speleothems as recorders of environmental change. *Quaternary Science Reviews*, *28*(5), 449–468. https://doi.org/10.1016/j.quascirev.2008.11.007

Frisia, S., Borsato, A., Drysdale, R. N., Paul, B., Greig, A., & Cotte, M. (2012). A re-evaluation of the palaeoclimatic significance of phosphorus variability in speleothems revealed by high-resolution synchrotron micro XRF mapping. *Climate of the Past*, *8*(6), 2039–2051. https://doi.org/10.5194/cp-8-2039-2012

Frisia, S. (2014). Microstratigraphic logging of calcite fabrics in speleothems as tool for palaeoclimate studies. *International Journal of Speleology*, *44*(1). https://doi.org/http://dx.doi.org/10.5038/1827-806X.44.1.1

Gámiz-Fortis, S. R., Pozo-Vázquez, D., Esteban-Parra, M. J., & Castro-Díez, Y. (2002). Spectral characteristics and predictability of the NAO assessed through Singular Spectral Analysis. *Journal of Geophysical Research: Atmospheres*, *107*(D23), ACL 11-1-ACL 11-15. https://doi.org/10.1029/2001JD001436

Garbe-Schönberg, D., & Müller, S. (2014). Nano-particulate pressed powder tablets for LA-ICP-MS. *Journal of Analytical Atomic Spectrometry*, *29*(6), 990–1000. https://doi.org/10.1039/C4JA00007B

Gerlitz, L., Steirou, E., Schneider, C., Moron, V., Vorogushyn, S., & Merz, B. (2018). Variability of the Cold Season Climate in Central Asia. Part I: Weather Types and Their Tropical and Extratropical Drivers. *Journal of Climate*, *31*(18), 7185–7207. https://doi.org/10.1175/JCLI-D-17-0715.1

Giorgi, F. (2006). Climate change hot-spots. *Geophysical Research Letters*, *33*(8). https://doi.org/10.1029/2006GL025734

Gong, D.-Y., & Ho, C.-H. (2002). The Siberian High and climate change over middle to high latitude Asia. *Theoretical and Applied Climatology*, *72*(1), 1–9. https://doi.org/10.1007/s007040200008

Grinsted, A., Moore, J. C., & Jevrejeva, S. (2004). Application of the cross wavelet transform and wavelet coherence to geophysical time series. *Nonlinear Processes in Geophysics*, *11*(5/6), 561–566.

Hao, Q., Wang, L., Oldfield, F., Peng, S., Qin, L., Song, Y., et al. (2012). Delayed build-up of Arctic ice sheets during 400,000-year minima in insolation variability. *Nature*, *490*(7420), 393–396. https://doi.org/10.1038/nature11493

Hellstrom, J. C., & McCulloch, M. T. (2000). Multi-proxy constraints on the climatic significance of trace element records from a New Zealand speleothem. *Earth and Planetary Science Letters*, *179*(2), 287–297. https://doi.org/10.1016/S0012-821X(00)00115-1

Hemming, S. R. (2004). Heinrich events: Massive late Pleistocene detritus layers of the North Atlantic and their global climate imprint. *Reviews of Geophysics*, *42*. https://doi.org/10.1029/2003RG000128

Hong, B., Gasse, F., Uchida, M., Hong, Y., Leng, X., Shibata, Y., et al. (2014). Increasing summer rainfall in arid eastern-Central Asia over the past 8500 years. *Scientific Reports*, *4*, 5279. https://doi.org/10.1038/srep05279

Huang, J., Guan, X., & Ji, F. (2012). Enhanced cold-season warming in semi-arid regions. *Atmospheric Chemistry and Physics*, *12*(12), 5391–5398. https://doi.org/10.5194/acp-12-5391-2012

Huang, X., Oberhänsli, H., von Suchodoletz, H., Prasad, S., Sorrel, P., Plessen, B., et al. (2014). Hydrological changes in western Central Asia (Kyrgyzstan) during the

Holocene as inferred from a palaeolimnological study in lake Son Kul. *Quaternary Science Reviews*, *103*, 134–152. https://doi.org/10.1016/j.quascirev.2014.09.012

Huang, X. Z., Chen, F. H., Fan, Y. X., & Yang, M. L. (2009). Dry late-glacial and early Holocene climate in arid central Asia indicated by lithological and palynological evidence from Bosten Lake, China. *Quaternary International*, *194*(1), 19–27. https://doi.org/10.1016/j.quaint.2007.10.002

Huang, Y., Fairchild, I. J., Borsato, A., Frisia, S., Cassidy, N. J., McDermott, F., & Hawkesworth, C. J. (2001). Seasonal variations in Sr, Mg and P in modern speleothems (Grotta di Ernesto, Italy). *Chemical Geology*, *175*(3), 429–448. https://doi.org/10.1016/S0009-2541(00)00337-5

Jaffey, A. H., Flynn, K. F., Glendenin, L. E., Bentley, W. C., & Essling, A. M. (1971). Precision Measurement of Half-Lives and Specific Activities of $^{235}\mathrm{U}$ and $^{238}\mathrm{U}$. *Physical Review C*, *4*(5), 1889–1906. https://doi.org/10.1103/PhysRevC.4.1889

Jin, L., Chen, F., Ganopolski, A., & Claussen, M. (2007). Response of East Asian climate to Dansgaard/Oeschger and Heinrich events in a coupled model of intermediate complexity. *Journal of Geophysical Research: Atmospheres*, *112*(D6). https://doi.org/10.1029/2006JD007316

Johnson, K. R., Hu, C., Belshaw, N. S., & Henderson, G. M. (2006). Seasonal trace-element and stable-isotope variations in a Chinese speleothem: The potential for high-resolution paleomonsoon reconstruction. *Earth and Planetary Science Letters*, *244*(1), 394–407. https://doi.org/10.1016/j.epsl.2006.01.064

Kalnay, E., Kanamitsu, M., Kistler, R., Collins, W., Deaven, D., Gandin, L., et al. (1996). The NCEP/NCAR 40-Year Reanalysis Project. *Bulletin of the American*

Meteorological Society, *77*(3), 437–472. https://doi.org/10.1175/1520-0477(1996)077<0437:TNYRP>2.0.CO;2

Laskar, J., Robutel, P., Joutel, F., Gastineau, M., Correia, A. C. M., & Levrard, B. (2004). A long-term numerical solution for the insolation quantities of the Earth. *Astronomy & Astrophysics*, *428*(1), 261–285. https://doi.org/10.1051/0004-6361:20041335

Lauterbach, S., Witt, R., Plessen, B., Dulski, P., Prasad, S., Mingram, J., et al. (2014). Climatic imprint of the mid-latitude Westerlies in the Central Tian Shan of Kyrgyzstan and teleconnections to North Atlantic climate variability during the last 6000 years. *The Holocene*, *24*(8), 970–984. https://doi.org/10.1177/0959683614534741

Li, Y., Song, Y., Lai, Z., Han, L., & An, Z. (2016). Rapid and cyclic dust accumulation during MIS 2 in Central Asia inferred from loess OSL dating and grain-size analysis. *Scientific Reports*, *6*, 32365. https://doi.org/10.1038/srep32365

Lin, J.-L. (2007). Interdecadal variability of ENSO in 21 IPCC AR4 coupled GCMs. *Geophysical Research Letters*, *34*(12). https://doi.org/10.1029/2006GL028937

Lioubimtseva, E., Cole, R., Adams, J. M., & Kapustin, G. (2005). Impacts of climate and land-cover changes in arid lands of Central Asia. *Journal of Arid Environments*, *62*(2), 285–308. https://doi.org/10.1016/j.jaridenv.2004.11.005

Lisiecki, L. E., & Raymo, M. E. (2005). A Pliocene-Pleistocene stack of 57 globally distributed benthic δ18O records. *Paleoceanography*, *20*(1). https://doi.org/10.1029/2004PA001071

Liu, X., Rao, Z., Shen, C.-C., Liu, J., Chen, J., Chen, S., et al. (2019). Holocene Solar Activity Imprint on Centennial- to Multidecadal-Scale Hydroclimatic Oscillations in

Arid Central Asia. *Journal of Geophysical Research: Atmospheres*, *124*(5), 2562–2573. https://doi.org/10.1029/2018JD029699

Lorens, R. B. (1981). Sr, Cd, Mn and Co distribution coefficients in calcite as a function of calcite precipitation rate. *Geochimica et Cosmochimica Acta*, *45*(4), 553–561. https://doi.org/10.1016/0016-7037(81)90188-5

Loulergue, L., Schilt, A., Spahni, R., Masson-Delmotte, V., Blunier, T., Lemieux, B., et al. (2008). Orbital and millennial-scale features of atmospheric CH_4 over the past 800,000 years. *Nature*, *453*(7193), 383–386. https://doi.org/10.1038/nature06950

Mackay, A. W., Swann, G. E. A., Fagel, N., Fietz, S., Leng, M. J., Morley, D., et al. (2013). Hydrological instability during the Last Interglacial in central Asia: a new diatom oxygen isotope record from Lake Baikal. *Quaternary Science Reviews*, *66*, 45–54. https://doi.org/10.1016/j.quascirev.2012.09.025

Mariotti, A. (2007). How ENSO impacts precipitation in southwest central Asia. *Geophysical Research Letters*, *34*(16). https://doi.org/10.1029/2007GL030078

Mathis, M., Sorrel, P., Klotz, S., Huang, X., & Oberhänsli, H. (2014). Regional vegetation patterns at lake Son Kul reveal Holocene climatic variability in central Tien Shan (Kyrgyzstan, Central Asia). *Quaternary Science Reviews*, *89*, 169–185. https://doi.org/10.1016/j.quascirev.2014.01.023

Mayewski, P. A., Meeker, L. D., Twickler, M. S., Whitlow, S., Yang, Q., Lyons, W. B., & Prentice, M. (1997). Major Features and Forcing of High-atitude Northern Hemisphere Atmospheric Circulation using a 110,000-year-long Glaciochemical Series. *Journal of Geophysical Research—Oceans*, *102*(C12), 26,345. https://doi.org/10.1029/96JC03365

McGarry, S. F., & Baker, A. (2000). Organic acid fluorescence: applications to speleothem palaeoenvironmental reconstruction. *Quaternary Science Reviews*, *19*(11), 1087–1101. https://doi.org/10.1016/S0277-3791(99)00087-6

Meeker, L. D., & Mayewski, P. A. (2002). A 1400-year high-resolution record of atmospheric circulation over the North Atlantic and Asia. *The Holocene*, *12*(3), 257–266. https://doi.org/10.1191/0959683602hl542ft

Mitchell, T. D., & Jones, P. D. (2005). An improved method of constructing a database of monthly climate observations and associated high-resolution grids - Mitchell - 2005 - International Journal of Climatology - Wiley Online Library. Retrieved June 13, 2019, from https://rmets.onlinelibrary.wiley.com/doi/10.1002/joc.1181

Murakami, T., Takamatsu, T., Katsuta, N., Takano, M., Yamamoto, K., Takahashi, Y., et al. (2012). Centennial- to millennial-scale climate shifts in continental interior Asia repeated between warm–dry and cool–wet conditions during the last three interglacial states: evidence from uranium and biogenic silica in the sediment of Lake Baikal, southeast Siberia. *Quaternary Science Reviews*, *52*, 49–59. https://doi.org/10.1016/j.quascirev.2012.08.001

Ozturk, T., Turp, M. T., Türkeş, M., & Kurnaz, M. L. (2017). Projected changes in temperature and precipitation climatology of Central Asia CORDEX Region 8 by using RegCM4.3.5. *Atmospheric Research*, *183*, 296–307. https://doi.org/10.1016/j.atmosres.2016.09.008

Paillard, D., Labeyrie, L., & Yiou, P. (n.d.). Macintosh program performs time-series analysis. *Eos Trans. AGU*, *77*(379).

Panagiotopoulos, F., Shahgedanova, M., Hannachi, A., & Stephenson, D. B. (2005). Observed Trends and Teleconnections of the Siberian High: A Recently Declining

Center of Action. *Journal of Climate*, *18*(9), 1411–1422. https://doi.org/10.1175/JCLI3352.1

Perșoiu, A., Ionita, M., & Weiss, H. (2019). Atmospheric blocking induced by the strengthened Siberian High led to drying in west Asia during the 4.2\,ka\,BP event — a hypothesis. *Climate of the Past*, *15*, 781–793. https://doi.org/10.5194/cp-15-781-2019

Prokopenko, A. A., Hinnov, L. A., Williams, D. F., & Kuzmin, M. I. (2006). Orbital forcing of continental climate during the Pleistocene: a complete astronomically tuned climatic record from Lake Baikal, SE Siberia. *Quaternary Science Reviews*, *25*(23), 3431–3457. https://doi.org/10.1016/j.quascirev.2006.10.002

Rossi, C., Bajo, P., Lozano, R. P., & Hellstrom, J. (2018). Younger Dryas to Early Holocene paleoclimate in Cantabria (N Spain): Constraints from speleothem Mg, annual fluorescence banding and stable isotope records. *Quaternary Science Reviews*, *192*, 71–85. https://doi.org/10.1016/j.quascirev.2018.05.025

Rudaya, N., Tarasov, P., Dorofeyuk, N., Solovieva, N., Kalugin, I., Andreev, A., et al. (2009). Holocene environments and climate in the Mongolian Altai reconstructed from the Hoton-Nur pollen and diatom records: a step towards better understanding climate dynamics in Central Asia. *Quaternary Science Reviews*, *28*(5–6), 540–554. https://doi.org/10.1016/j.quascirev.2008.10.013

Rutlidge, H., Baker, A., Marjo, C. E., Andersen, M. S., Graham, P. W., Cuthbert, M. O., et al. (2014). Dripwater organic matter and trace element geochemistry in a semi-arid karst environment: Implications for speleothem paleoclimatology. *Geochimica et Cosmochimica Acta*, *135*, 217–230. https://doi.org/10.1016/j.gca.2014.03.036

Sanding, A., & Bruno, J. (1992). The solubility of (UO2)3(PO4)2 · 4H2O(s) and the formation of U(VI) phosphate complexes: Their influence in uranium speciation in natural waters. *Geochimica et Cosmochimica Acta*, *56*(12), 4135–4145. https://doi.org/10.1016/0016-7037(92)90256-I

Schwarz, A., Turner, F., Lauterbach, S., Plessen, B., Krahn, K. J., Glodniok, S., et al. (2017). Mid- to late Holocene climate-driven regime shifts inferred from diatom, ostracod and stable isotope records from Lake Son Kol (Central Tian Shan, Kyrgyzstan). *Quaternary Science Reviews*, *177*, 340–356. https://doi.org/10.1016/j.quascirev.2017.10.009

Shakun, J. D., Clark, P. U., He, F., Marcott, S. A., Mix, A. C., Liu, Z., et al. (2012). Global warming preceded by increasing carbon dioxide concentrations during the last deglaciation. *Nature*, *484*(7392), 49–54. https://doi.org/10.1038/nature10915

de Sherbinin, A. (2014). Climate change hotspots mapping: what have we learned? *Climatic Change*, *123*(1), 23–37. https://doi.org/10.1007/s10584-013-0900-7

Stoll, H. M., Müller, W., & Prieto, M. (2012). I-STAL, a model for interpretation of Mg/Ca, Sr/Ca and Ba/Ca variations in speleothems and its forward and inverse application on seasonal to millennial scales: I-STAL SPELEOTHEM TRACE ELEMENT MODEL. *Geochemistry, Geophysics, Geosystems*, *13*(9). https://doi.org/10.1029/2012GC004183

Sun, Y., Clemens, S. C., Morrill, C., Lin, X., Wang, X., & An, Z. (2012). Influence of Atlantic meridional overturning circulation on the East Asian winter monsoon. *Nature Geoscience*, *5*(1), 46–49. https://doi.org/10.1038/ngeo1326

Syed, F. S., Giorgi, F., Pal, J. S., & King, M. P. (2006). Effect of remote forcings on the winter precipitation of central southwest Asia part 1: observations. *Theoretical and Applied Climatology*, *86*(1), 147–160. https://doi.org/10.1007/s00704-005-0217-1

Syed, F. S., Giorgi, F., Pal, J. S., & Keay, K. (2009). Regional climate model simulation of winter climate over Central-Southwest Asia, with emphasis on NAO and ENSO effects. *International Journal of Climatology*, n/a-n/a. https://doi.org/10.1002/joc.1887

Tan, M., Baker, A., Genty, D., Smith, C., Esper, J., & Cai, B. (2006). Applications of stalagmite laminae to paleoclimate reconstructions: Comparison with dendrochronology/climatology. *Quaternary Science Reviews*, *25*(17), 2103–2117. https://doi.org/10.1016/j.quascirev.2006.01.034

Tesoriero, A. J., & Pankow, J. F. (1996). Solid solution partitioning of Sr2+, Ba2+, and Cd2+ to calcite. *Geochimica et Cosmochimica Acta*, *60*(6), 1053–1063. https://doi.org/10.1016/0016-7037(95)00449-1

Treble, P., Shelley, J. M. G., & Chappell, J. (2003). Comparison of high resolution sub-annual records of trace elements in a modern (1911–1992) speleothem with instrumental climate data from southwest Australia. *Earth and Planetary Science Letters*, *216*(1), 141–153. https://doi.org/10.1016/S0012-821X(03)00504-1

Tremaine, D. M., & Froelich, P. N. (2013). Speleothem trace element signatures: A hydrologic geochemical study of modern cave dripwaters and farmed calcite. *Geochimica et Cosmochimica Acta*, *121*, 522–545. https://doi.org/10.1016/j.gca.2013.07.026

Williams, M. W., & Konovalov, V. G. (2008). Central Asia Temperature and Precipitation Data, 1879-2003, Version 1. *NSIDC: National Snow and Ice Data Center*.

Wolff, C., Plessen, B., Dudashvilli, A. S., Breitenbach, S. F., Cheng, H., Edwards, L. R., & Strecker, M. R. (2017). Precipitation evolution of Central Asia during the last 5000 years. *The Holocene*, *27*(1), 142–154. https://doi.org/10.1177/0959683616652711